Joint analysis of Dark Energy Survey Year 3 data and CMB lensing from SPT and Planck. II. Cross-correlation measurements and cosmologicalconstraints

C. Chang,[1,2] Y. Omori,[1,2,3,4] E. J.Baxter,[5] C. Doux,[6] A. Choi,[7] S. Pandey,[6] A. Alarcon,[8] O. Alves,[9,10] A. Amon,[4] F. Andrade-Oliveira,[9] K. Bechtol,[11] M. R. Becker,[8] G. M. Bernstein,[6] F. Bianchini,[3,4,12] J. Blazek,[13,14] L. E. Bleem,[8,2] H. Camacho,[15,10] A. Campos,[16] A. Carnero Rosell,[10,17,18] M. Carrasco Kind,[19,20] R. Cawthon,[21] R. Chen,[22] J. Cordero,[23] T. M. Crawford,[1,2] M. Crocce,[24,25] C. Davis,[4] J. DeRose,[26] S. Dodelson,[16,27] A. Drlica-Wagner,[1,2,28] K. Eckert,[6] T. F.Eifler,[29,30] F. Elsner,[31] J. Elvin-Poole,[32,33] S. Everett,[34] X. Fang,[29,35] A. Ferté,[30] P. Fosalba,[24,25] O. Friedrich,[36] M. Gatti,[6] G. Giannini,[37] D. Gruen,[38] R. A. Gruendl,[19,20] I. Harrison,[23,39,40] K. Herner,[28] H. Huang,[29,41] E. M. Huff,[30] D. Huterer,[9] M. Jarvis,[6] A. Kovacs,[17,18] E. Krause,[29] N. Kuropatkin,[28] P.-F.Leget,[4] P. Lemos,[31,42] A. R. Liddle,[43] N. MacCrann,[44] J. McCullough,[4] J. Muir,[45] J. Myles,[3,4,46] A. Navarro-Alsina,[47] Y. Park,[48] A. Porredon,[32,33] J. Prat,[1,2] M. Raveri,[6] R. P. Rollins,[23] A. Roodman,[4,46] R. Rosenfeld,[10,49] A. J. Ross,[32] E. S. Rykoff,[4,46] C. Sánchez,[6] J. Sanchez,[28] L. F. Secco,[2] I. Sevilla-Noarbe,[50] E. Sheldon,[51] T. Shin,[6] M. A. Troxel,[22] I. Tutusaus,[24,25,52] T. N. Varga,[53,54] N. Weaverdyck,[9,26] R. H. Wechsler,[3,4,46] W. L. K. Wu,[4,46] B. Yanny,[28] B. Yin,[16] Y. Zhang,[28] J. Zuntz,[55] T. M. C. Abbott,[56] M. Aguena,[10] S. Allam,[28] J. Annis,[28] D. Bacon,[57] B. A. Benson,[1,2,28] E. Bertin,[58,59] S. Bocquet,[60] D. Brooks,[31] D. L. Burke,[4,46] J. E.Carlstrom,[1,2,8,61,62] J. Carretero,[37] C. L. Chang,[1,2,8] R. Chown,[63,64] M. Costanzi,[65,66,67] L. N. da Costa,[10,68] A. T. Crites,[1,2,69] M. E. S.Pereira,[70] T. de Haan,[71,72] J. De Vicente,[50] S. Desai,[73] H. T. Diehl,[28] M. A. Dobbs,[74,75] P. Doel,[31] W. Everett,[76] I. Ferrero,[77] B. Flaugher,[28] D. Friedel,[19] J. Frieman,[2,28] J. García-Bellido,[78] E. Gaztanaga,[24,25] E. M. George,[79,72] T. Giannantonio,[36,80] N. W. Halverson,[76,81] S. R. Hinton,[82] G. P.Holder,[20,75,83] D. L. Hollowood,[34] W. L. Holzapfel,[72] K. Honscheid,[32,33] J. D. Hrubes,[84] D. J. James,[85] L. Knox,[86] K. Kuehn,[87,88] O. Lahav,[31] A. T. Lee,[26,89] M. Lima,[10,90] D. Luong-Van,[84] M. March,[6] J. J.McMahon,[1,2,61,62] P. Melchior,[91] F. Menanteau,[19,20] S. S.Meyer,[1,2,61,92] R. Miquel,[37,93] L. Mocanu,[1,2] J. J. Mohr,[94,95,96] R. Morgan,[11] T. Natoli,[1,2] S. Padin,[1,2,97] A. Palmese,[35] F. Paz-Chinchón,[19,80] A. Pieres,[10,68] A. A. Plazas Malagón,[91] C. Pryke,[98] C. L. Reichardt,[12] M. Rodríguez-Monroy,[50] A. K. Romer,[42] J. E. Ruhl,[99] E. Sanchez,[50] K. K. Schaffer,[2,61,100] M. Schubnell,[9] S. Serrano,[24,25] E. Shirokoff,[1,2] M. Smith,[101] Z. Staniszewski,[99,30] A. A. Stark,[102] E. Suchyta,[103] G. Tarle,[9] D. Thomas,[57] C. To,[32] J. D. Vieira,[20,83] J. Weller,[53,54] and R. Williamson[104,1,2]

(DES & SPT Collaborations)

[1]Department of Astronomy and Astrophysics, University of Chicago, Chicago, Illinois 60637, USA
[2]Kavli Institute for Cosmological Physics, University of Chicago, Chicago, Illinois 60637, USA
[3]Department of Physics, Stanford University, 382 Via Pueblo Mall, Stanford, California 94305, USA
[4]Kavli Institute for Particle Astrophysics & Cosmology,
P. O. Box 2450, Stanford University, Stanford, California 94305, USA
[5]Institute for Astronomy, University of Hawai'i, 2680 Woodlawn Drive, Honolulu, Hawaii 96822, USA
[6]Department of Physics and Astronomy, University of Pennsylvania,
Philadelphia, Pennsylvania 19104, USA
[7]California Institute of Technology, 1200 East California Blvd,
MC 249-17, Pasadena, California 91125, USA
[8]Argonne National Laboratory, 9700 South Cass Avenue, Lemont, Illinois 60439, USA
[9]Department of Physics, University of Michigan, Ann Arbor, Michigan 48109, USA
[10]Laboratório Interinstitucional de e-Astronomia - LIneA,
Rua Gal. José Cristino 77, Rio de Janeiro, RJ - 20921-400, Brazil
[11]Physics Department, 2320 Chamberlin Hall, University of Wisconsin-Madison,
1150 University Avenue Madison, Wisconsin 53706-1390
[12]School of Physics, University of Melbourne, Parkville, Victoria 3010, Australia
[13]Department of Physics, Northeastern University, Boston, Massachusetts 02115, USA
[14]Laboratory of Astrophysics, École Polytechnique Fédérale de Lausanne (EPFL),
Observatoire de Sauverny, 1290 Versoix, Switzerland
[15]Instituto de Física Teórica, Universidade Estadual Paulista, São Paulo, Brazil
[16]Department of Physics, Carnegie Mellon University, Pittsburgh, Pennsylvania 15312, USA
[17]Instituto de Astrofisica de Canarias, E-38205 La Laguna, Tenerife, Spain
[18]Universidad de La Laguna, Dpto. Astrofísica, E-38206 La Laguna, Tenerife, Spain

[19]Center for Astrophysical Surveys, National Center for Supercomputing Applications,
1205 West Clark St., Urbana, Illinois 61801, USA
[20]Department of Astronomy, University of Illinois at Urbana-Champaign,
1002 W. Green Street, Urbana, Illinois 61801, USA
[21]Physics Department, William Jewell College, Liberty, Missouri, 64068
[22]Department of Physics, Duke University, Durham, North Carolina 27708, USA
[23]Jodrell Bank Center for Astrophysics, School of Physics and Astronomy, University of Manchester,
Oxford Road, Manchester, M13 9PL, United Kingdom
[24]Institut d'Estudis Espacials de Catalunya (IEEC), 08034 Barcelona, Spain
[25]Institute of Space Sciences (ICE, CSIC),
Campus UAB, Carrer de Can Magrans, s/n, 08193 Barcelona, Spain
[26]Lawrence Berkeley National Laboratory, 1 Cyclotron Road, Berkeley, California 94720, USA
[27]NSF AI Planning Institute for Physics of the Future, Carnegie Mellon University,
Pittsburgh, Pennsylvania 15213, USA
[28]Fermi National Accelerator Laboratory, P. O. Box 500, Batavia, Illinois 60510, USA
[29]Department of Astronomy/Steward Observatory, University of Arizona,
933 North Cherry Avenue, Tucson, Arizona 85721-0065, USA
[30]Jet Propulsion Laboratory, California Institute of Technology,
4800 Oak Grove Drive, Pasadena, California 91109, USA
[31]Department of Physics & Astronomy, University College London,
Gower Street, London, WC1E 6BT, United Kingdom
[32]Center for Cosmology and Astro-Particle Physics, The Ohio State University,
Columbus, Ohio 43210, USA
[33]Department of Physics, The Ohio State University, Columbus, Ohio 43210, USA
[34]Santa Cruz Institute for Particle Physics, Santa Cruz, California 95064, USA
[35]Department of Astronomy, University of California,
Berkeley, 501 Campbell Hall, Berkeley, California 94720, USA
[36]Kavli Institute for Cosmology, University of Cambridge,
Madingley Road, Cambridge CB3 0HA, United Kingdom
[37]Institut de Física d'Altes Energies (IFAE), The Barcelona Institute of Science and Technology,
Campus UAB, 08193 Bellaterra (Barcelona) Spain
[38]University Observatory, Faculty of Physics, Ludwig-Maximilians-Universitat,
Scheinerstrasse 1, 81679 Munich, Germany
[39]Department of Physics, University of Oxford,
Denys Wilkinson Building, Keble Road, Oxford OX1 3RH, United Kingdom
[40]School of Physics and Astronomy, Cardiff University, CF24 3AA, United Kingdom
[41]Department of Physics, University of Arizona, Tucson, Arizona 85721, USA
[42]Department of Physics and Astronomy, Pevensey Building, University of Sussex,
Brighton, BN1 9QH, United Kingdom
[43]Instituto de Astrofísica e Ciências do Espaço, Faculdade de Ciências, Universidade de Lisboa,
1769-016 Lisboa, Portugal
[44]Department of Applied Mathematics and Theoretical Physics, University of Cambridge,
Cambridge CB3 0WA, United Kingdom
[45]Perimeter Institute for Theoretical Physics, 31 Caroline St. North, Waterloo, Ontario N2L 2Y5, Canada
[46]SLAC National Accelerator Laboratory, Menlo Park, California 94025, USA
[47]Instituto de Física Gleb Wataghin, Universidade Estadual de Campinas,
13083-859, Campinas, SP, Brazil
[48]Kavli Institute for the Physics and Mathematics of the Universe (WPI), UTIAS, The University of Tokyo,
Kashiwa, Chiba 277-8583, Japan
[49]ICTP South American Institute for Fundamental Research Instituto de Física Teórica,
Universidade Estadual Paulista, São Paulo, Brazil
[50]Centro de Investigaciones Energéticas, Medioambientales y Tecnológicas (CIEMAT), Madrid, Spain
[51]Brookhaven National Laboratory, Bldg 510, Upton, New York 11973, USA
[52]Département de Physique Théorique and Center for Astroparticle Physics, Université de Genève,
24 quai Ernest Ansermet, CH-1211 Geneva, Switzerland
[53]Max Planck Institute for Extraterrestrial Physics, Giessenbachstrasse, 85748 Garching, Germany
[54]Universitäts-Sternwarte, Fakultät für Physik, Ludwig-Maximilians Universität München,
Scheinerstrasse 1, 81679 München, Germany
[55]Institute for Astronomy, University of Edinburgh, Edinburgh EH9 3HJ, United Kingdom

[56]Cerro Tololo Inter-American Observatory, NSF's National Optical-Infrared Astronomy Research Laboratory, Casilla 603, La Serena, Chile

[57]Institute of Cosmology and Gravitation, University of Portsmouth, Portsmouth, PO1 3FX, United Kingdom

[58]CNRS, UMR 7095, Institut d'Astrophysique de Paris, F-75014, Paris, France

[59]Sorbonne Universités, UPMC Univ Paris 06, UMR 7095, Institut d'Astrophysique de Paris, F-75014, Paris, France

[60]Ludwig-Maximilians-Universität, Scheiner- strasse 1, 81679 Munich, Germany

[61]Enrico Fermi Institute, University of Chicago, 5640 South Ellis Avenue, Chicago, Illinois 60637, USA

[62]Department of Physics, University of Chicago, 5640 South Ellis Avenue, Chicago, Illinois 60637, USA

[63]Department of Physics & Astronomy, The University of Western Ontario, London Ontario N6A 3K7, Canada

[64]Institute for Earth and Space Exploration, The University of Western Ontario, London Ontario N6A 3K7, Canada

[65]Astronomy Unit, Department of Physics, University of Trieste, via Tiepolo 11, I-34131 Trieste, Italy

[66]INAF-Osservatorio Astronomico di Trieste, via G. B. Tiepolo 11, I-34143 Trieste, Italy

[67]Institute for Fundamental Physics of the Universe, Via Beirut 2, 34014 Trieste, Italy

[68]Observatório Nacional, Rua Gal. José Cristino 77, Rio de Janeiro, RJ - 20921-400, Brazil

[69]Department of Astronomy & Astrophysics, University of Toronto, 50 St George St, Toronto, Ontario, M5S 3H4, Canada

[70]Hamburger Sternwarte, Universität Hamburg, Gojenbergsweg 112, 21029 Hamburg, Germany

[71]High Energy Accelerator Research Organization (KEK), Tsukuba, Ibaraki 305-0801, Japan

[72]Department of Physics, University of California, Berkeley, California 94720, USA

[73]Department of Physics, IIT Hyderabad, Kandi, Telangana 502285, India

[74]Department of Physics and McGill Space Institute, McGill University, 3600 Rue University, Montreal, Quebec H3A 2T8, Canada

[75]Canadian Institute for Advanced Research, CIFAR Program in Gravity and the Extreme Universe, Toronto, Ontario M5G 1Z8, Canada

[76]Department of Astrophysical and Planetary Sciences, University of Colorado, Boulder, Colorado 80309, USA

[77]Institute of Theoretical Astrophysics, University of Oslo, P.O. Box 1029 Blindern, NO-0315 Oslo, Norway

[78]Instituto de Fisica Teorica UAM/CSIC, Universidad Autonoma de Madrid, 28049 Madrid, Spain

[79]European Southern Observatory, Karl-Schwarzschild-Straße 2, 85748 Garching, Germany

[80]Institute of Astronomy, University of Cambridge, Madingley Road, Cambridge CB3 0HA, United Kingdom

[81]Department of Physics, University of Colorado, Boulder, Colorado, 80309, USA

[82]School of Mathematics and Physics, University of Queensland, Brisbane, QLD 4072, Australia

[83]Department of Physics, University of Illinois Urbana-Champaign, 1110 West Green Street, Urbana, Illinois 61801, USA

[84]University of Chicago, 5640 South Ellis Avenue, Chicago, Illinois 60637, USA

[85]Center for Astrophysics | Harvard & Smithsonian, 60 Garden Street, Cambridge, Massachusetts 02138, USA

[86]Department of Physics, University of California, One Shields Avenue, Davis, California 95616, USA

[87]Australian Astronomical Optics, Macquarie University, North Ryde, New South Wales 2113, Australia

[88]Lowell Observatory, 1400 Mars Hill Rd, Flagstaff, Arizona 86001, USA

[89]Department of Physics, University of California, Berkeley, California, 94720, USA

[90]Departamento de Física Matemática, Instituto de Física, Universidade de São Paulo, CP 66318, São Paulo, SP, 05314-970, Brazil

[91]Department of Astrophysical Sciences, Princeton University, Peyton Hall, Princeton, New Jersey 08544, USA

[92]Department of Physics, University of Chicago, 5640 South Ellis Avenue, Chicago, Illinois, 60637, USA

[93]Institució Catalana de Recerca i Estudis Avançats, E-08010 Barcelona, Spain

[94]Ludwig-Maximilians-Universität, Scheiner- str.1, 81679 Munich, Germany

[95]Excellence Cluster Universe, Boltzmannstr 2, 85748 Garching, Germany

[96]Max-Planck-Institut fur extraterrestrische Physik, Giessenbachstrasse 85748 Garching, Germany

[97]California Institute of Technology, 1200 East California Boulevard, Pasadena, California 91125, USA

[98]School of Physics and Astronomy, University of Minnesota, 116 Church Street SE Minneapolis, Minnesota 55455, USA

[99]Department of Physics, Case Western Reserve University, Cleveland, Ohio 44106, USA

[100] Liberal Arts Department, School of the Art Institute of Chicago, Chicago, Illinois USA 60603
[101] School of Physics and Astronomy, University of Southampton,
Southampton SO17 1BJ, United Kingdom
[102] Harvard-Smithsonian Center for Astrophysics,
60 Garden Street, Cambridge, Massachusetts 02138, USA
[103] Computer Science and Mathematics Division, Oak Ridge National Laboratory,
Oak Ridge, Tennessee 37831
[104] Jet Propulsion Laboratory, California Institute of Technology, Pasadena, California 91109, USA

Cross-correlations of galaxy positions and galaxy shears with maps of gravitational lensing of the cosmic microwave background (CMB) are sensitive to the distribution of large-scale structure in the Universe. Such cross-correlations are also expected to be immune to some of the systematic effects that complicate correlation measurements internal to galaxy surveys. We present measurements and modeling of the cross-correlations between galaxy positions and galaxy lensing measured in the first three years of data from the Dark Energy Survey with CMB lensing maps derived from a combination of data from the 2500 deg^2 SPT-SZ survey conducted with the South Pole Telescope and full-sky data from the Planck satellite. The CMB lensing maps used in this analysis have been constructed in a way that minimizes biases from the thermal Sunyaev Zel'dovich effect, making them well suited for cross-correlation studies. The total signal-to-noise of the cross-correlation measurements is 23.9 (25.7) when using a choice of angular scales optimized for a linear (nonlinear) galaxy bias model. We use the cross-correlation measurements to obtain constraints on cosmological parameters. For our fiducial galaxy sample, which consist of four bins of magnitude-selected galaxies, we find constraints of $\Omega_m = 0.272^{+0.032}_{-0.052}$ and $S_8 \equiv \sigma_8 \sqrt{\Omega_m / 0.3} = 0.736^{+0.032}_{-0.028}$ ($\Omega_m = 0.245^{+0.026}_{-0.044}$ and $S_8 = 0.734^{+0.035}_{-0.028}$) when assuming linear (nonlinear) galaxy bias in our modeling. Considering only the cross-correlation of galaxy shear with CMB lensing, we find $\Omega_m = 0.270^{+0.043}_{-0.061}$ and $S_8 = 0.740^{+0.034}_{-0.029}$. Our constraints on S_8 are consistent with recent cosmic shear measurements, but lower than the values preferred by primary CMB measurements from Planck.

I. INTRODUCTION

Significant progress has been made recently in using cross-correlations between galaxy imaging and cosmic microwave background (CMB) surveys to constrain cosmological parameters. These developments have come naturally as ongoing galaxy and CMB surveys collect increasingly sensitive data across larger and larger overlapping areas of the sky. The Dark Energy Survey [DES, 1] is the largest galaxy weak lensing survey today, covering ~5000 deg^2 of sky that is mostly in the southern hemisphere. By design, the DES footprint overlaps with high-resolution CMB observations from the South Pole Telescope [SPT, 2], enabling a large number of cross-correlation analyses [3–12].

Although CMB photons originate from the high-redshift Universe, their trajectories are deflected by low-redshift structures as a result of gravitational lensing—these are the same structures traced by the distributions of galaxies and the galaxy weak lensing signal measured in optical galaxy surveys. Cross-correlating CMB lensing with galaxy surveys therefore allows us to extract information stored in the large-scale structure.

In this work, we analyze both $\langle \delta_g \kappa_{CMB} \rangle$, the cross correlation of the galaxy density field δ_g and the CMB weak lensing convergence field κ_{CMB}, and $\langle \gamma \kappa_{CMB} \rangle$,[1] the cross correlation of the galaxy weak lensing shear field γ and κ_{CMB}. Notably, these two two-point functions correlate measurements from very different types of surveys (galaxy surveys in the optical and CMB surveys in the millimeter), and are therefore expected to be very robust to systematic biases impacting only one type of survey. Furthermore, CMB lensing is sensitive to a broad range of redshift, with peak sensitivity at redshift $z \sim 2$; galaxy lensing, on the other hand, is sensitive to structure at $z \lesssim 1$ for current surveys. As a result, the CMB lensing cross-correlation functions, $\langle \delta_g \kappa_{CMB} \rangle + \langle \gamma_t \kappa_{CMB} \rangle$, are expected to increase in signal-to-noise relative to galaxy lensing correlations as one considers galaxy samples that extend to higher redshift.

Our analysis relies on the first three years (Y3) of galaxy observations from DES and a CMB lensing map constructed using data from the 2500 deg^2 SPT-SZ survey [13]

---

[1] The "t" subscript denotes the tangential component of shear, which will be discussed in Sec. V.

and Planck [14]. The combined signal-to-noise of the $\langle \delta_g \kappa_{CMB} \rangle$ þ $\langle \gamma_t \kappa_{CMB} \rangle$ measurements used in the present cosmological analysis is roughly a factor two larger than in the earlier DES þ SPT results presented in [11], which used first year (Y1) DES data. This large improvement in signal-to-noise derives from two main advancements:

(1) We have adopted a different methodology in constructing the CMB lensing map, which results in much lower contamination from the thermal Sunyaev Zel'dovich (tSZ) effect, allowing small-scale information to be used in the cosmological analysis. This methodology is described in [15].

(2) Data from DES Y3 covers an area approximately three times larger than DES Y1 and is slightly deeper.

Along with the significant increase in signal-to-noise, we have also updated our models for the correlation functions to include a number of improvements following [16]. These include an improved treatment of galaxy intrinsic alignments, inclusion of magnification effects on the lens galaxy density, and application of the so-called lensing ratio likelihood described in [17].

The analysis presented here is the second of a series of three papers: In [15] (Paper I) we describe the construction of the combined, tSZ-cleaned SPT þ Planck CMB lensing map and the methodology for the cosmological analysis. In this paper (Paper II), we present the data measurements of the cross-correlation probes $\langle \delta_g \kappa_{CMB} \rangle$ þ $\langle \gamma_t \kappa_{CMB} \rangle$, a series of diagnostic tests, and cosmological constraints from this cross-correlation combination. In [18] (Paper III), we will present the joint cosmological constraints from $\langle \delta_g \kappa_{CMB} \rangle$ þ $\langle \gamma_t \kappa_{CMB} \rangle$ and the DES-only 3 × 2 pt probes,[2] and tests of consistency between the two, as well as constraints from a joint analysis with the CMB lensing auto-spectrum.

Similar analyses have recently been carried out using different galaxy imaging surveys and CMB data. [19] studied the cross-correlation of the galaxy weak lensing from the Hyper Suprime-Cam Subaru Strategic Program Survey [HSC-SSP, 20] and the Planck lensing map [21]; [22] used the same HSC galaxy weak lensing measurement to cross-correlate with CMB lensing from the POLARBEAR experiment [23]; [24] cross-correlated galaxy weak lensing from the Kilo-Degree Survey [KiDS, 25] and the CMB lensing map from the Atacama Cosmology Telescope [ACT, 26]; and [27] cross-correlated the galaxy density measured in unWISE data [28] with Planck CMB lensing. Compared to these previous studies, in addition to the new datasets, this paper is unique in that we combine $\langle \delta_g \kappa_{CMB} \rangle$ and $\langle \gamma_t \kappa_{CMB} \rangle$. Moreover, our analysis uses the same modeling choices and analysis framework as in [16], making it easy to compare and combine our results later (i.e. Paper III).

The structure of the paper is as follows. In Sec. II we briefly review the formalism of our model for the two cross-correlation functions and the parameter inference pipeline (more details can be found in Paper I). In Sec. III we review the data products used in this analysis. In Sec. IV we introduce the estimators we use for the correlation functions. In Sec. V we describe out blinding procedure and unblinding criteria. In Sec. VI we present constraints on cosmological parameters as well as relevant nuisance parameters when fitting to the cross-correlation functions. Finally we conclude in Sec. VII.

II. MODELING AND INFERENCE

We follow the theoretical formalism laid out in Paper I and [29] for this work. Here, we summarize only the main equations relevant to this paper. Following standard convention, we refer to the galaxies used to measure δ_g as lens galaxies, and the galaxies used to measure γ as source galaxies.

Angular power spectra: Using the Limber approximation[3] [31], the cross-spectra between CMB lensing convergence and galaxy density/shear can be related to the matter power spectrum via:

$$C^{\kappa_{CMB}X^i}(l) = \int d\chi \frac{q_{\kappa_{CMB}}(\chi) q_X^i(\chi)}{\chi^2} P_{NL}\left(\frac{l+1/2}{\chi}; z(\chi)\right); \tag{1}$$

where $X \in \{\delta_g, \gamma\}$, i labels the redshift bin, $P_{NL}(k; z)$ is the nonlinear matter power spectrum, which we compute using CAMB and HALOFIT [32,33], and χ is the comoving distance to redshift z. The weighting functions $q_X(\chi)$, describe how the different probes respond to large-scale structure at different distances and are given by

$$q_{\kappa_{CMB}}(\chi) = \frac{3\Omega_m H_0^2}{2c^2} \frac{\chi}{a(\chi)} \frac{\chi_* - \chi}{\chi_*}; \tag{2}$$

$$q_{\delta_g}^i(\chi) = b^i n_{\delta_g}^i(z(\chi)) \frac{dz}{d\chi}; \tag{3}$$

$$q_\gamma^i(\chi) = \frac{3H_0^2 \Omega_m}{2c^2} \frac{\chi}{a(\chi)} \int_\chi^{\chi_h} d\chi' n_\gamma^i(z(\chi')) \frac{dz}{d\chi'} \frac{\chi' - \chi}{\chi'}; \tag{4}$$

---

[2] The 3 × 2 pt probes refer to a combination of three two-point functions of the galaxy density field δ_g and the weak lensing shear field γ: galaxy clustering $\langle \delta_g \delta_g \rangle$, galaxy-galaxy lensing $\langle \delta_g \gamma \rangle$ and cosmic shear $\langle \gamma \gamma \rangle$.

[3] In [30], the authors showed that at DES Y3 accuracy, the Limber approximation is sufficient for galaxy-galaxy lensing and cosmic shear, but insufficient for galaxy clustering. Given the primary probe in this work, $\langle \delta_g \kappa_{CMB} \rangle$ þ $\langle \gamma_t \kappa_{CMB} \rangle$, are at much lower signal-to-noise than galaxy-galaxy lensing and cosmic shear, we expect that Limber approximation is still a valid choice.

where H_0 and Ω_m are the Hubble constant and matter density parameters, respectively, $a(\chi)$ is the scale factor corresponding to comoving distance χ, χ_* denotes the comoving distance to the surface of last scattering, $b(z)$ is the galaxy bias as a function of redshift, and $n^i(z)$ are the normalized redshift distributions of the lens/source galaxies in bin i. We note that the above equations assumes linear galaxy bias, which is our fiducial model. Modeling the nonlinear galaxy bias involves changes to both Eq. (1) and Eq. (3) (see below).

Correlation functions: The angular-space correlation functions are then computed via

$$w^{\delta_g \kappa_{CMB}}(\theta) = \sum_l \frac{2l+1}{4\pi} F(l) P_l (\cos(\theta)) C_l^{\delta_g \kappa_{CMB}}(l); \qquad (5)$$

$$w^{\gamma_t \kappa_{CMB}}(\theta) = \sum_l \frac{2l+1}{4\pi l(l+1)} F(l) P_l^2 (\cos\theta) C_l^{\gamma \kappa_{CMB}}(l); \qquad (6)$$

where P_l and P_l^2 are the lth order Legendre polynomial and associated Legendre polynomial, respectively, and $F(l)$ describes filtering applied to the κ_{CMB} maps. For correlations with the κ_{CMB} maps, we set $F(l) = B(l) H(l - l_{min}) H(l_{max} - l)$, where $H(l)$ is a step function, and $B(l) = \exp(-0.5 l(l+1)\sigma^2)$ with $\sigma \equiv \frac{\theta_{FWHM}}{\sqrt{8 \ln 2}}$ and θ_{FWHM} describes the beam applied to the CMB lensing maps (see discussion of l_{min}, l_{max}, and θ_{FWHM} choices in Sec. III, and further discussion in Paper I).

Galaxy bias: We consider two models for the galaxy bias. Our fiducial choice is a linear bias model where $b(z) = b$ is not a function of scale and is assumed to be a free parameter for each tomographic bin i. The second bias model is described in [34] and is an effective 1-loop model with renormalized nonlinear galaxy bias parameters b_1^i (linear bias), b_2^i (local quadratic bias), $b_{s^2}^i$ (tidal quadratic bias) and b_{3nl}^i (third-order non-local bias). The latter two parameters can be derived from b_1^i, making the total number of free parameters for this bias model two per tomographic bin i. To use this model, we replace the combination of $b^2 P_{NL}$ in Equation (1) with P_{gm} described in [34].

Intrinsic alignment (IA): Galaxy shapes can be intrinsically aligned as a result of nearby galaxies evolving in a common tidal field. IA modifies the observed lensing signal. We adopt the five-parameter ($a_1, a_2, \eta_1, \eta_2, b_{ta}$) tidal alignment tidal torquing model (TATT) of [35] to describe galaxy IA. a_1 and η_1 characterize the amplitude and redshift dependence of the tidal alignment; a_2 and η_2 characterize the amplitude and redshift dependence of the tidal torquing effect; b_{ta} accounts for the fact that our measurement is weighted by the observed galaxy counts. In Sec. VI B, we will also compare our results using a simpler IA model, the nonlinear alignment model

[NLA, 36]. The TATT model is equivalent to the NLA model in the limit that $a_2 = \eta_2 = b_{ta} = 0$.

Impact of lensing magnification on lens galaxy density: Foreground structure modulates the observed galaxy density as a result of gravitational magnification. The effect of magnification can be modeled by modifying Eq. (3) to include the change in selection and geometric dilution quantified by the lensing bias coefficients C_g^i:

$$q_{\delta_g}^i(\chi) \to q_{\delta_g}^i(\chi)(1 + C_g^i \kappa_g^i); \qquad (7)$$

where κ_g is the tomographic convergence field, as described in [29] and the values of C_g^i are estimated in [37] and fixed to the values listed in Table I.

Uncertainty in redshift distributions: We model uncertainty in the redshift distributions of the source galaxies with shift parameters Δz^i, defined such that for each redshift bin i,

$$n^i(z) \to n^i(z - \Delta_z^i): \qquad (8)$$

For the lens sample, we additionally introduce a stretch parameter (σ_z^i) when modeling the redshift distribution, as motivated by [38]:

$$n^i(z) \to \sigma_z^i n^i(\sigma_z^i [z - \langle z \rangle] + \langle z \rangle - \Delta_z^i); \qquad (9)$$

where $\langle z \rangle$ is the mean redshift.

Uncertainty in shear calibration: We model uncertainty in the shear calibration with multiplicative factors defined such that the observed $C_l^{\kappa_{CMB} \gamma}$ is modified by

$$C_l^{\kappa_{CMB} \gamma^i}(l) \to (1 + m^i) C_l^{\kappa_{CMB} \gamma^i}(l); \qquad (10)$$

where m^i is the shear calibration bias for source bin i.

Lensing ratio (or shear ratio, SR): The DES Y3 3 × 2 pt analysis used a ratio of small-scale galaxy lensing measurements to provide additional information, particularly on source galaxy redshift biases and on IA parameters. These ratios are not expected to directly inform the cosmological constraints; they can, however, improve constraints via degeneracy breaking with nuisance parameters. The lensing ratios can therefore be considered as another form of systematic calibration, in a similar vein to, e.g., spectroscopic data used to calibrate redshifts, and image simulations used to calibrate shear biases. In [17], it was demonstrated that the lensing ratio measurements are approximately independent of the 3 × 2 pt measurements, making it trivial to combine constraints from 3 × 2 pt and lensing ratios at the likelihood level. Unless otherwise mentioned, all our analyses will include the information from these lensing ratios. We investigate their impact in Sec. VI B.

Angular scale cuts: The theoretical model described above is uncertain on small scales due to uncertainty in our understanding of baryonic feedback and the galaxy-halo

TABLE I. Prior values for cosmological and nuisance parameters included in our model. For the priors, $U[a, b]$ indicates a uniform prior between a and b, while $N(a, b)$ indicates a Gaussian prior with mean a and standard deviation b. $\delta(a)$ is a Dirac Delta function at value a, which effectively means that the parameter is fixed at a. Note that the fiducial lens sample is the first 4 bins of the MAGLIM sample. The two high-redshift MAGLIM bins and the REDMAGIC sample are shown in gray to indicate they are not part of the fiducial analysis.

Parameter	Prior
Ω_m	$U[0.1, 0.9]$
$A_s \times 10^9$	$U[0.5, 5.0]$
n_s	$U[0.87, 1.07]$
Ω_b	$U[0.03, 0.07]$
h	$U[0.55, 0.91]$
$\Omega_\nu h^2 \times 10^4$	$U[6.0, 64.4]$
a_1	$U[-5.0, 5.0]$
a_2	$U[-5.0, 5.0]$
η_1	$U[-5.0, 5.0]$
η_2	$U[-5.0, 5.0]$
b_{ta}	$U[0.0, 2.0]$
MAGLIM	
b^{16}	$U[0.8, 3.0]$
b_1^{16}	$U[0.67, 3.0]$
b_2^{16}	$U[-4.2, 4.2]$
C_l^{16}	$\delta(1.21), \delta(1.15), \delta(1.88), \delta(1.97), \delta(1.78),$ $\delta(2.48)$
$\Delta_z^{1\dots6} \times 10^2$	$N(-0.9, 0.7), N(-3.5, 1.1), N(-0.5, 0.6),$ $N(-0.7, 0.6), N(0.2, 0.7), N(0.2, 0.8)$
$\sigma_z^{1\dots6}$	$N(0.98, 0.062), N(1.31, 0.093),$ $N(0.87, 0.054), N(0.92, 0.05),$ $N(1.08, 0.067), N(0.845, 0.073)$
REDMAGIC	
b^{15}	$U[0.8, 3.0]$
b_1^{15}	$U[0.67, 2.52]$
b_2^{15}	$U[-3.5, 3.5]$
C_l^{15}	$\delta(1.31), \delta(-0.52), \delta(0.34), \delta(2.25), \delta(1.97)$
$\Delta_z^{1\dots5} \times 10^2$	$N(0.6, 0.4), N(0.1, 0.3), N(0.4, 0.3),$ $N(-0.2, 0.5), N(-0.7, 1.0)$
$\sigma_z^{1\dots4}$	$\delta(1), \delta(1), \delta(1), \delta(1), N(1.23, 0.054)$
METACALIBRATION	
$m^{1\dots4} \times 10^3$	$N(-6.0, 9.1), N(-20.0, 7.8), N(-24.0, 7.6),$ $N(-37.0, 7.6)$
$\Delta_z^{1\dots4} \times 10^{-2}$	$N(0.0, 1.8), N(0.0, 1.5), N(0.0, 1.1),$ $N(0.0, 1.7)$

connection (or, nonlinear galaxy bias). We take the approach of only fitting the correlation functions on angular scales we can reliably model. In Paper I we determined the corresponding angular scale cuts by requiring the cosmological constraints to not be significantly biased when prescriptions for unmodeled effects are introduced. In Figs. 2 and 19 the scale cuts are marked by the gray bands.

Parameter inference: We assume a Gaussian likelihood[4] for the data vector of measured correlation functions, $\vec{d}$, given a model $\vec{m}$, generated using the set of parameters $\vec{p}$

$$\ln L(\vec{d}|\vec{m}(\vec{p})) = -\frac{1}{2}\sum_{ij}^{N}(d_i - m_i(\vec{p}))C_{ij}^{-1}(d_j - m_j(\vec{p})),$$

(11)

where the sums run over all of the N elements in the data and model vectors. The posterior on the model parameters is then given by:

$$P(\vec{m}(\vec{p})|\vec{d}) \propto L(\vec{d}|\vec{m}(\vec{p}))P_{prior}(\vec{p}),$$

(12)

where $P_{prior}(\vec{p})$ is a prior on the model parameters. Our choice of priors is summarized in Table I.

The covariance matrix used here consists of an analytical lognormal covariance combined with empirical noise estimation from simulations. The covariance has been extensively validated in Paper I. In Appendix A Fig. 11 we show that the diagonal elements of our final analytic covariance are in excellent agreement with a covariance estimated from data using jackknife resampling.

Our modeling and inference framework is built within the COSMOSIS package [40] and is designed to be consistent with those developed as part of [16]. We generate parameter samples using the nested sampler POLYCHORD [41].

III. DATA

A. CMB lensing maps

There are two major advances in the galaxy and CMB data used here relative to the DES Y1 and SPT analysis presented in [9,10]. First, for the CMB map in the SPT footprint, we used the method developed in [42] and described in Paper I to remove contamination from the tSZ effect by combining data from SPT and Planck. Such contamination was one of the limiting factors in our Y1 analysis. Second, the DES Y3 data cover a significantly larger area on the sky than the DES Y1 data. Consequently, the DES Y3 footprint extends beyond the SPT footprint, necessitating the use of the Planck-only lensing map [14] over part of the DES Y3 patch. As discussed in Paper I, the different noise properties and filtering of the two lensing maps necessitates separate treatment throughout. The "SPT þ Planck" lensing map, which overlaps with the DES footprint at < -40 degrees in declination, is filtered by $l_{min} = 8$, $l_{max} = 5000$ and a Gaussian smoothing of $\theta_{FWHM} = 6$ arcmin. This map is produced using the combination of 150 GHz data from the 2500 deg^2 SPT-SZ survey [e.g., 13], Planck 143 GHz data, and the

---

[4]See e.g., [39] for tests of the validity of this assumption in the context of cosmic shear, which would also apply here.

tSZ-cleaned CMB Planck temperature map generated using the Spectral Matching Independent Component Analysis (SMICA) algorithm (i.e. the SMICA-noSZ map). The "Planck" lensing map, which overlaps with the DES footprint at > −39.5 degrees in declination, is filtered by $l_{min} = 8$, $l_{max} = 3800$ and a Gaussian smoothing of $\theta_{FWHM} = 8$ arcmin is applied. This map is reconstructed using the Planck SMICA-noSZ temperature map alone. We leave a small 0.5 deg gap between the two lensing maps to reduced the correlation between structures on the boundaries. The resulting effective overlapping areas with DES are 1764 deg^2 and 2156 deg^2 respectively for the SPT + Planck and Planck patches respectively.

B. The DES Y3 data products

DES [43] is a photometric survey in five broadband filters (grizY), with a footprint of nearly 5000 deg^2 of sky that is mostly in the southern hemisphere, imaging hundreds of millions of galaxies. It employs the 570-megapixel Dark Energy Camera [DECam, 1] on the Cerro Tololo Inter-American Observatory (CTIO) 4 m Blanco telescope in Chile. We use data from the first three years (Y3) of DES observations. The foundation of the various DES Y3 data products is the Y3 Gold catalog described in [44], which achieves S=N ~ 10 for extended objects up to i ~ 23.0 over an unmasked area of 4143 deg^2. In this work we use three galaxy samples: two lens samples for the galaxy density-CMB lensing correlation, h$\delta_g\kappa_{CMB}$i, and one source sample for the galaxy shear-CMB lensing correlation, h$\gamma\kappa_{CMB}$i. We briefly describe each sample below. These samples are the same as those used in [16] and we direct the readers to a more detailed description of the samples therein.

1. Lens samples: MAGLIM and REDMAGIC

We will show results from two lens galaxy samples named MAGLIM and REDMAGIC. Following [16], the first four bins of the MAGLIM sample will constitute our fiducial sample, though we show results from the other bins and samples to help understand potential systematic effects in the DES galaxy selection.

The MAGLIM sample consists of 10.7 million galaxies selected with a magnitude cut that evolves linearly with the photometric redshift estimate: i < 4z_{phot} + 18. z_{phot} is determined using the Directional Neighborhood Fitting algorithm [DNF, 45]. [46] optimized the magnitude cut to balance the statistical power of the sample size and the accuracy of the photometric redshifts for cosmological constraints from galaxy clustering and galaxy-galaxy lensing. MAGLIM is divided into six tomographic bins. The top panel of Fig. 1 shows the per-bin redshift distributions, which have been validated using cross-correlations with spectroscopic galaxies in [38]. Weights are derived to account for survey systematics, as described in [47].
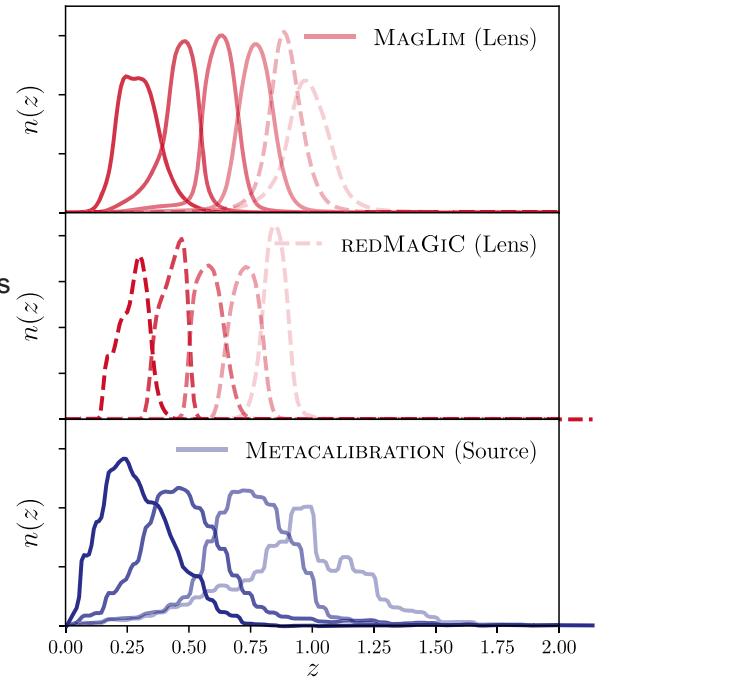

FIG. 1. Redshift distribution for the tomographic bins for the galaxy samples used in this work: the MAGLIM lens sample (top), the REDMAGIC lens sample (middle), and the METACAL source sample (bottom). The fiducial lens sample only uses the first four bins of the MAGLIM sample, or the solid lines. We perform tests with the nonfiducial samples (dashed lines) for diagnostic purposes.

The REDMAGIC sample consists of 2.6 million luminous red galaxies (LRGs) with small photometric redshift errors [48]. REDMAGIC is constructed using a red sequence template calibrated via the REDMAPPER algorithm [49,50]. The lens galaxies are divided into five tomographic bins. The redshift distributions are shown in the middle panel of Fig. 1. These distributions are estimated using draws from the redshift probability distribution functions of the individual REDMAGIC galaxies. As with MAGLIM, [38] validates the redshift distributions, and [47] derives systematics weights.

We note that in [16] the two high-redshift bins were excluded in MAGLIM due to poor fits in the 3 × 2 pt analysis, while the REDMAGIC sample was excluded due to an internal tension between galaxy-galaxy lensing and galaxy clustering. With the addition of CMB lensing cross-correlations, one of the aims of this work will be to shed light on potential systematic effects in the lens samples. We briefly discuss this issue in Sec. VI D but there will be a more in-depth discussion in Paper III when we combine with the 3 × 2 pt probes.

2. Source sample: METACALIBRATION

For the source sample, we use the DES Y3 shear catalog presented in [51], which contains over 100 million galaxies.

The galaxy shapes are estimated using the METACALIBRATION algorithm [52,53]. The shear catalog has been thoroughly tested in [51,54]. In [54], the authors used realistic image simulations to constrain the multiplicative bias of the shear estimate to be at most 2%–3%, primarily attributed to a shear-dependent detection bias coupled with object blending effects. The residual shear calibration biases are folded into the modeling pipeline and are listed in Table I.

The source galaxies are divided into four tomographic bins based on the SOMPZ algorithm described in [55], utilizing deep field data described in [56] and image simulations described in [57]. The bottom panel of Fig. 1 shows the redshift distributions, which have been validated in [58,17].

IV. CORRELATION FUNCTION ESTIMATORS

Our estimator for the galaxy-CMB lensing correlation [Eq. (5)] is

$$\langle \delta_g \kappa_{CMB}(\theta_\alpha) \rangle = \langle \delta_g \kappa_{CMB}(\theta_\alpha) \rangle_0 - \langle \delta_R \kappa_{CMB}(\theta_\alpha) \rangle; \quad (13)$$

where

$$\langle \delta_g \kappa_{CMB}(\theta_\alpha) \rangle_0 = \frac{1}{N_{\theta_\alpha}^{\delta_g \kappa_{CMB}}} \sum_{i=1}^{N_g} \sum_{j=1}^{N_{pix}} \eta_i^{\delta_g} \eta_j^{\kappa_{CMB}} \kappa_{CMB;j} \, \Theta_\alpha(\hat{\theta}^i - \hat{\theta}^j) \quad (14)$$

and

$$\langle \delta_R \kappa_{CMB}(\theta_\alpha) \rangle = \frac{1}{N_{\theta_\alpha}^{R\kappa_{CMB}}} \sum_{i=1}^{N_{rand}} \sum_{j=1}^{N_{pix}} \eta_i^{\delta_R} \eta_j^{\kappa_{CMB}} \kappa_{CMB;j} \, \Theta_\alpha(\hat{\theta}^i - \hat{\theta}^j); \quad (15)$$

where the sum in i is over all galaxies and the sum in j is over all pixels in the CMB convergence map; $N_{\theta_\alpha}^{\delta_g \kappa_{CMB}}$ $(N_{\theta_\alpha}^{\delta_R \kappa_{CMB}})$ is the number of galaxy-κ_{CMB} pixel (random-κ_{CMB} pixel) pairs that fall within the angular bin θ_α; η^{δ_g}, η^{δ_R} and $\eta^{\kappa_{CMB}}$ are the weights associated with the galaxies, the randoms and the κ_{CMB} pixels. The weights for the galaxies/randoms are derived in Rodríguez-Monroy [47] using a combination of maps of survey properties (e.g., seeing, depth, airmass) to correct for any spurious signals in the large-scale structure, while the κ_{CMB} weights account for differences in the noise levels of pixels in the κ_{CMB} map. The random catalog is used to sample the selection function of the lens galaxies, and has a number density much higher than the galaxies. $\hat{\theta}^i$ $(\hat{\theta}^j)$ is the angular position of galaxy i (pixel j), and Θ_α is an indicator function that is 1 if $|\hat{\theta}^i - \hat{\theta}^j|$ falls in the angular bin θ_α and 0 otherwise.

Our estimator for the galaxy shear-CMB lensing correlation [Eq. (6)] is

$$\langle \gamma_t \kappa_{CMB}(\theta_\alpha) \rangle = \frac{\sum_{i=1}^{N_{gal}} \sum_{j=1}^{N_{pix}} \eta_i^e \eta_j^{\kappa_{CMB}} \kappa_{CMB;j} \, e_t^{ij} \, \Theta_\alpha(\hat{\theta}^i - \hat{\theta}^j)}{s(\theta_\alpha) \sum \eta_i^e \eta_j^{\kappa_{CMB}}}; \quad (16)$$

where e_t^{ij} is the component of the corrected ellipticity oriented orthogonally to the line connecting pixel j and the source galaxy. The κ_{CMB} value in the pixel is κ_{CMB} and η_i^e and $\eta_j^{\kappa_{CMB}}$ are the weights associated with the source galaxy and the κ_{CMB} pixel, respectively. The weights for the source galaxies are derived in Gatti et al. [51] and combines the signal-to-noise and size of each galaxy. $s(\theta)$ is the METACALIBRATION response. We find that $s(\theta)$ is approximately constant over the angular scales of interest, but different for each redshift bin. We carry out these measurements using the TREECORR package [59] in the angular range $2.5^0 < \theta < 250.0^0$. Note that Eq. (16) does not require subtracting a random component as in Eq. (13) since unlike a density field, the mask geometry cannot generate an artificial signal in a shear field.

The measured MAGLIM $\langle \delta_g \kappa_{CMB} \rangle$ and $\langle \gamma_t \kappa_{CMB} \rangle$ correlation functions are shown in Fig. 2. The $\langle \delta_g \kappa_{CMB} \rangle$ measurements using the REDMAGIC sample are shown in Appendix C. The signal-to-noise (S/N) of the different measurements are listed in Table II. Here, signal-to-noise is calculated via

$$S/N \equiv \sqrt{\sum_{ij}^{N} d_i^T C_{ij}^{-1} d_j}; \quad (17)$$

where d is the data vector of interest and C is the covariance matrix. The final signal-to-noise of the fiducial $\langle \delta_g \kappa_{CMB} \rangle$ þ $\langle \gamma_t \kappa_{CMB} \rangle$ data vector after the linear bias scale cuts is 23.9, about two times larger than in the Y1 study [11]—the main improvement, in addition to the increased sky area, comes from extending our analysis to smaller scales, enabled by the tSZ-cleaned CMB lensing map. The tSZ signal is correlated with large-scale structure, and can propagate into a bias in the estimated κ_{CMB} if not mitigated. In the DES Y1 analysis presented in [11], tSZ cleaning was not implemented at the κ_{CMB} map level, necessitating removal of small-scale CMB lensing correlation measurements from the model fits. This problem was particularly severe for $\langle \gamma_t \kappa_{CMB} \rangle$. Comparing results for the SPT þ Planck and Planck patches in Table II, the SPT þ Planck area dominates the signal-to-noise before scale cuts in all the probes, even with a smaller sky area. This is due to the lower noise level of the SPT maps. However, since the higher signal-to-

---

[5]https://github.com/rmjarvis/TreeCorr.
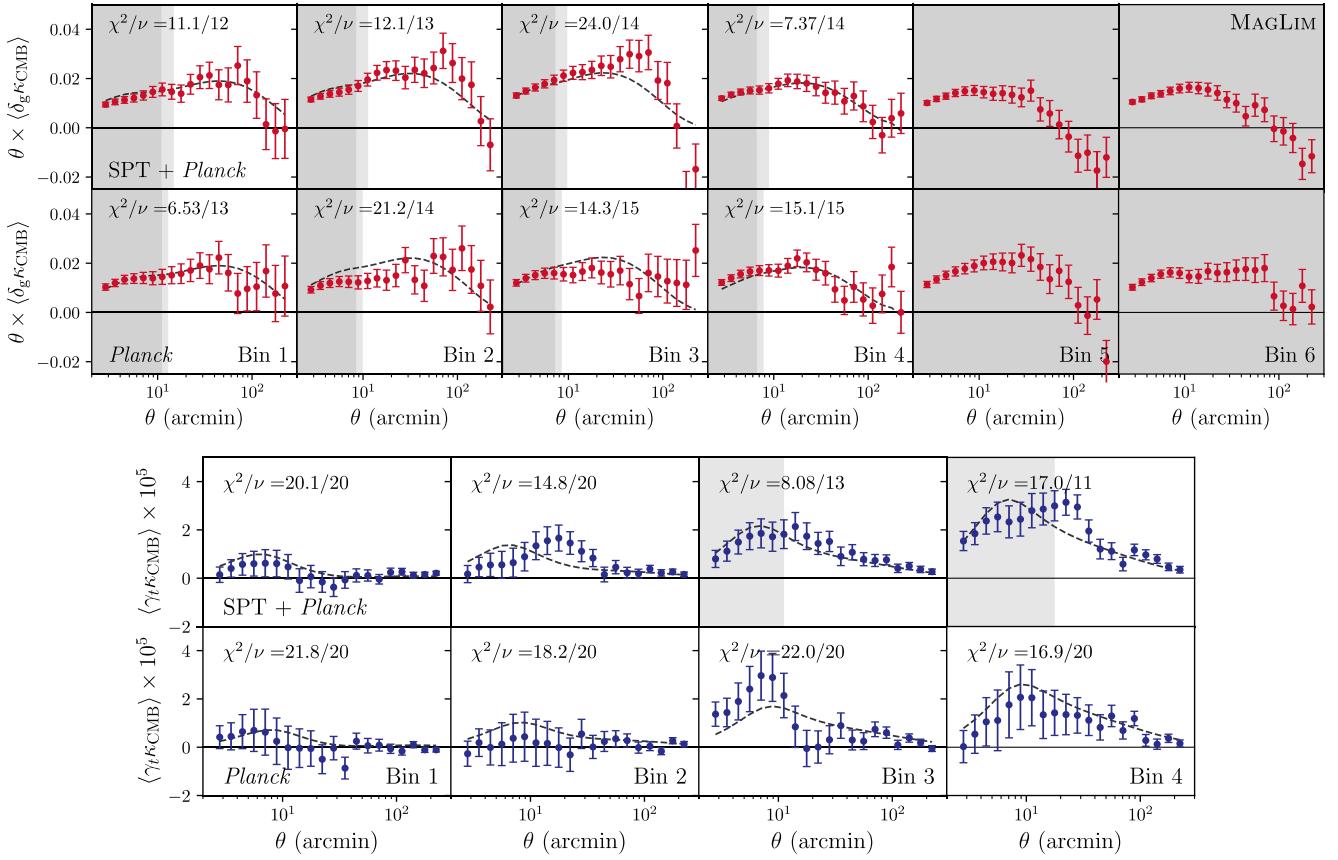
FIG. 2.   Measurement of the MAGLIM galaxy density-CMB lensing correlation (top) and galaxy shear-CMB lensing correlation (bottom). For each set of measurements, the upper row shows measurement with the SPT þ Planck CMB lensing map and the lower row shows measurement with the Planck CMB lensing map. The shapes and amplitudes are different due to the difference in the L cut and smoothing of the CMB lensing map. The light (dark) shaded regions in the $\langle \delta_g \kappa_{CMB} \rangle$ panels indicate the data points removed when assuming linear (nonlinear) galaxy bias, while the shaded regions in the $\langle \gamma_t \kappa_{CMB} \rangle$ panels show the data points removed in all cases (only two bins require scale cuts). The dashed dark gray line shows the best-fit fiducial model for the fiducial lens sample, while the χ^2 per degree of freedom (ν) evaluated at the best-fit model with scale cuts for linear galaxy bias model is shown in the upper left corner of each panel.

noise necessitates a more stringent scale cut, the resulting signal-to-noise after scale cuts is only slightly higher for the SPT þ Planck patch. Finally, comparing $\langle \delta_g \kappa_{CMB} \rangle$ and $\langle \gamma_t \kappa_{CMB} \rangle$, even though $\langle \delta_g \kappa_{CMB} \rangle$ starts with ~75% more signal-to-noise before scale cuts compared to $\langle \gamma_t \kappa_{CMB} \rangle$, the scale cuts remove significantly more signal in $\langle \delta_g \kappa_{CMB} \rangle$ compared to $\langle \gamma_t \kappa_{CMB} \rangle$. This is due to limits in our ability to model nonlinear galaxy bias on small scales—indeed we see that the signal-to-noise in $\langle \delta_g \kappa_{CMB} \rangle$ increases by 13% when switching from linear to nonlinear galaxy bias model. Overall, these signal-to-noise levels are consistent with the forecasts in Paper I.

V. BLINDING AND UNBLINDING

Following [16], we adopt a strict, multilevel blinding procedure in our analysis designed to minimize the impact of experimenter bias. The first level of blinding occurs at the shear catalog level, where all shears are multiplied by a secret factor [51]. The second level of blinding occurs at the two-point function level, where we follow the procedure outlined in [60] and shift the data vectors by an unknown amount while maintaining the degeneracy between the different parts of the data vector under the same cosmology. The main analyses in this paper were conducted after the unblinding of the shear catalog, so the most relevant blinding step is the data vector blinding. Below we outline the list of tests that were used to determine whether our measurement is sufficiently robust to unblind:

(i) Pass all tests described in Appendix B, which indicate no outstanding systematic contamination in the data vectors. These tests include: (1) check for spurious correlation of our signal with survey property maps, (2) check the cross-shear component of $\langle \gamma_t \kappa_{CMB} \rangle$, (3) check the impact of weights used for the lens galaxies, (4) check the effect of the point-source mask in the CMB lensing map on our measurements, and (5) check that cross-correlating an external large-scale

TABLE II. Signal-to-noise for the different parts of the $\langle \delta_g \kappa_{CMB} \rangle + \langle \gamma_t \kappa_{CMB} \rangle$ data vector when different scale cuts are applied. Rows involving the two high-redshift MAGLIM bins and the REDMAGIC sample are shown in gray to indicate that they are not part of the fiducial analysis.

Scale cuts		None	Linear bias	Nonlinear bias
SPT + Planck				
$\langle \delta_g \kappa_{CMB} \rangle$	MAGLIM	26.8	14.5	17.3
$\langle \delta_g \kappa_{CMB} \rangle$	MAGLIM 6 bin	30.2	17.4	20.0
$\langle \delta_g \kappa_{CMB} \rangle$	REDMAGIC	23.7	14.2	15.7
$\langle \gamma_t \kappa_{CMB} \rangle$	MAGLIM	15.0	13.4	13.4
Planck				
$\langle \delta_g \kappa_{CMB} \rangle$	MAGLIM	17.9	13.1	13.8
$\langle \delta_g \kappa_{CMB} \rangle$	MAGLIM 6 bin	20.5	15.9	16.8
$\langle \delta_g \kappa_{CMB} \rangle$	REDMAGIC	17.0	12.5	12.8
$\langle \gamma_t \kappa_{CMB} \rangle$	MAGLIM	10.4	10.4	10.4
Combined				
$\langle \delta_g \kappa_{CMB} \rangle$	MAGLIM	32.2	19.6	22.2
$\langle \gamma_t \kappa_{CMB} \rangle$	MAGLIM	18.2	16.9	16.9
$\langle \delta_g \kappa_{CMB} \rangle + \langle \gamma_t \kappa_{CMB} \rangle$	MAGLIM	34.8	23.9	25.7

structure tracer (the cosmic infrared background in this case) with different versions of our CMB lensing maps yields consistent results.

(ii) With unblinded chains, use the posterior predictive distribution (PPD) method developed in [61] to evaluate the consistency between the two subsets of the data vectors that use different CMB lensing maps (i.e. the SPT + Planck patch and the Planck patch). The p-value should be larger than 0.01.

(iii) With unblinded chains, verify that the goodness-of-fit of the data with respect to the fiducial model has a p-value larger than 0.01 according to the same PPD framework.

Except for the first step, all the above are applied to the $\langle \delta_g \kappa_{CMB} \rangle + \langle \gamma_t \kappa_{CMB} \rangle$ data vectors with the fiducial analysis choices (ΛCDM cosmology and linear galaxy bias scale cuts), for the first four bins of the MAGLIM lens sample.

VI. PARAMETER CONSTRAINTS FROM CROSS-CORRELATIONS OF DES WITH CMB LENSING

Following the steps outlined in the previous section, we found (1) no evidence for significant systematic biases in our measurements as shown in Appendix B, (2) we obtain a p-value greater than 0.01 when comparing the $\langle \delta_g \kappa_{CMB} \rangle + \langle \gamma_t \kappa_{CMB} \rangle$ constraints from the Planck region to constraints from the SPT + Planck region, and (3) the goodness-of-fit test of the fiducial $\langle \delta_g \kappa_{CMB} \rangle + \langle \gamma_t \kappa_{CMB} \rangle$ unblinded chain has a p-value greater than 0.01. In the following, we will quote the precise p-values obtained from these tests using the updated covariance matrix.

With all the unblinding tests passed, we froze all analysis choices and unblinded our cosmological constraints. We then updated the covariance matrix to match the best-fit parameters from the cosmological analysis.[6] The results we present below use the updated covariance matrix. The main constraints on cosmological parameters are summarized in Table III.

A. Cosmological constraints from cross-correlations

In Fig. 3 we show constraints from $\langle \delta_g \kappa_{CMB} \rangle + \langle \gamma_t \kappa_{CMB} \rangle$ using the first 4 bins of the MAGLIM sample. For comparison, we also show constraints from $\langle \gamma_t \kappa_{CMB} \rangle$-only, cosmic shear (from [62,63]), and 3 × 2 pt (from [16]).

We find that our analysis of $\langle \delta_g \kappa_{CMB} \rangle + \langle \gamma_t \kappa_{CMB} \rangle$ gives the following constraints:

$$\Omega_m = 0.272^{+0.032}_{-0.052};$$
$$\sigma_8 = 0.781^{+0.073}_{-0.073};$$
$$S_8 = 0.736^{+0.032}_{-0.028}.$$

As can be seen from Fig. 3 and expected from Paper I, the constraints are dominated by $\langle \gamma_t \kappa_{CMB} \rangle$, with $\langle \delta_g \kappa_{CMB} \rangle$ slightly improving the Ω_m constraints. While $\langle \delta_g \kappa_{CMB} \rangle$ by itself does not tightly constrain cosmology because of the degeneracy with galaxy bias, the shape information in $\langle \delta_g \kappa_{CMB} \rangle$ provides additional information on Ω_m when combined with $\langle \gamma_t \kappa_{CMB} \rangle$.

Figure 3 also shows constraints from DES-only probes, including cosmic shear and 3 × 2 pt. We find that the constraints on S_8 from $\langle \delta_g \kappa_{CMB} \rangle + \langle \gamma_t \kappa_{CMB} \rangle$ are comparable to those from cosmic shear and 3 × 2 pt, and in reasonable agreement. The uncertainties of the $\langle \delta_g \kappa_{CMB} \rangle + \langle \gamma_t \kappa_{CMB} \rangle$ constraints on S_8 are roughly 30% (70%) larger than that of cosmic shear (3 × 2 pt). We will perform a complete assessment of consistency between these probes in Paper III. We can also see that the degeneracy direction of the $\langle \delta_g \kappa_{CMB} \rangle + \langle \gamma_t \kappa_{CMB} \rangle$ constraints are slightly different from 3 × 2 pt, which will help in breaking degeneracies when combined.

We consider constraints from the SPT + Planck and Planck patches separately in Fig. 4. As discussed earlier in Sec. V, the consistency of these two patches was part of the unblinding criteria, thus these two constraints are consistent

---

[6]This procedure is the same as in [16]. Since we cannot know the cosmological and nuisance parameters exactly before running the full inference, a set of fiducial parameters were used to generate the first-pass of the covariance that was used for all blinded chains. After unblinding, we update the parameters to values closer to the best-fit parameters from the data. After confirming that the 5 × 2 pt best-fit constraints Paper III are consistent with the 3 × 2 pt best-fit constraints, we chose to use the 3 × 2 pt best-fit parameters for evaluating the covariance matrix, as this makes our modeling choices more consistent with that of [16].

TABLE III. ΛCDM constraints on Ω_m, σ_8 and S_8 using $\langle \delta_g \kappa_{CMB} \rangle + \langle \gamma_t \kappa_{CMB} \rangle$ and different lens samples. We show the constraints using both linear and nonlinear galaxy bias. The last column shows the p-value corresponding to the goodness of fit for the chain. The parts shown in gray indicate that they are not part of the fiducial samples.

Dataset		σ_8	Ω_m	S_8	PPD p-value
$\langle \gamma_t \kappa_{CMB} \rangle$	MAGLIM	$0.790^{+0.080}_{-0.092}$	$0.270^{+0.043}_{-0.061}$	$0.740^{+0.034}_{-0.029}$	0.72
$\langle \delta_g \kappa_{CMB} \rangle + \langle \gamma_t \kappa_{CMB} \rangle$	MAGLIM 4 bin linear galaxy bias	$0.781^{+0.073}_{-0.073}$	$0.272^{+0.032}_{-0.052}$	$0.736^{+0.032}_{-0.028}$	0.50
$\langle \delta_g \kappa_{CMB} \rangle + \langle \gamma_t \kappa_{CMB} \rangle$	MAGLIM 4 bin nonlinear galaxy bias	$0.820^{+0.079}_{-0.067}$	$0.245^{+0.026}_{-0.044}$	$0.734^{+0.035}_{-0.028}$	0.51
$\langle \delta_g \kappa_{CMB} \rangle + \langle \gamma_t \kappa_{CMB} \rangle$	MAGLIM 6 bin linear galaxy bias	$0.755^{+0.071}_{-0.071}$	$0.288^{+0.037}_{-0.053}$	$0.732^{+0.032}_{-0.029}$	0.45
$\langle \delta_g \kappa_{CMB} \rangle + \langle \gamma_t \kappa_{CMB} \rangle$	MAGLIM 6 bin nonlinear galaxy bias	$0.769^{+0.071}_{-0.071}$	$0.273^{+0.034}_{-0.047}$	$0.727^{+0.035}_{-0.035}$	0.45
$\langle \delta_g \kappa_{CMB} \rangle + \langle \gamma_t \kappa_{CMB} \rangle$	REDMAGIC linear galaxy bias	$0.793^{+0.072}_{-0.083}$	$0.266^{+0.036}_{-0.050}$	$0.738^{+0.034}_{-0.030}$	0.39
$\langle \delta_g \kappa_{CMB} \rangle + \langle \gamma_t \kappa_{CMB} \rangle$	REDMAGIC nonlinear galaxy bias	$0.794^{+0.069}_{-0.069}$	$0.253^{+0.030}_{-0.046}$	$0.723^{+0.033}_{-0.030}$	0.41

under the PPD metric. We find a p-value of 0.37 (0.33) when comparing the Planck (SPT + Planck) results to constraints from SPT + Planck (Planck). We also observe that the constraints are somewhat tighter in the SPT + Planck patch in S_8, consistent with the slightly larger signal-to-noise (see Table II). We note however, that the signal-to-noise before scale cuts of the SPT + Planck patch is significantly larger than the Planck patch due to the lower noise and smaller beam size of the SPT lensing map (for $\langle \delta_g \kappa_{CMB} \rangle$: 26.8 vs. 17.9; for $\langle \gamma_t \kappa_{CMB} \rangle$: 15.0 vs. 10.4), though most of the signal-to-noise is on the small scales which we had to remove due to uncertainties in the theoretical modeling. This highlights the importance of improving the small-scale modeling in future work.

B. Lensing ratio and IA modeling

As discussed in Sec. II, we have included the lensing ratio likelihood in all our constraints. As was investigated in detail in [17], the inclusion of the lensing ratio information mainly constrains the IA parameters and source galaxy redshift biases. The TATT IA model adopted here is a general and flexible model that allows for a large range of possible IA contributions. As such, it is expected that including the lensing ratio could have a fairly large impact for data vectors that are not already constraining the IA parameters well. We now examine the effect of the lensing ratio on our fiducial $\langle \delta_g \kappa_{CMB} \rangle + \langle \gamma_t \kappa_{CMB} \rangle$ constraints by first removing the lensing ratio prior in our fiducial result, and then doing the same comparison with a different,
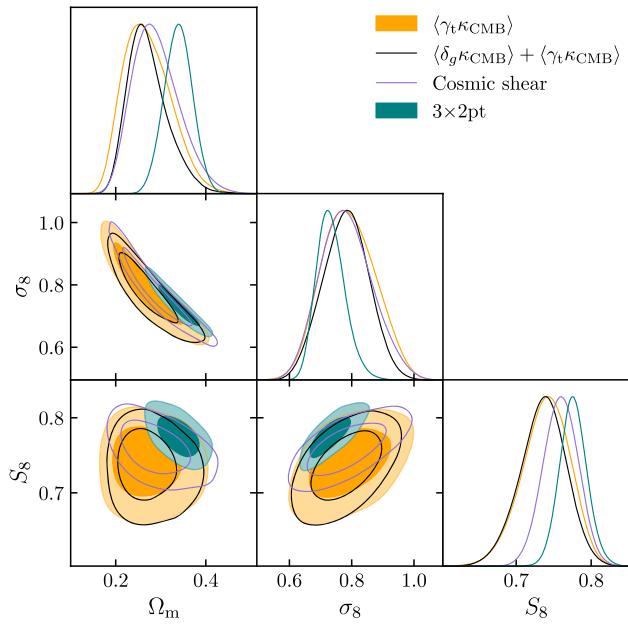

FIG. 3.   Constraints on cosmological parameters Ω_m, σ_8, and S_8 from $\langle \delta_g \kappa_{CMB} \rangle + \langle \gamma_t \kappa_{CMB} \rangle$ using the MAGLIM sample. We also show the corresponding constraints from $\langle \gamma_t \kappa_{CMB} \rangle$-only, cosmic shear and 3 × 2pt for comparison.
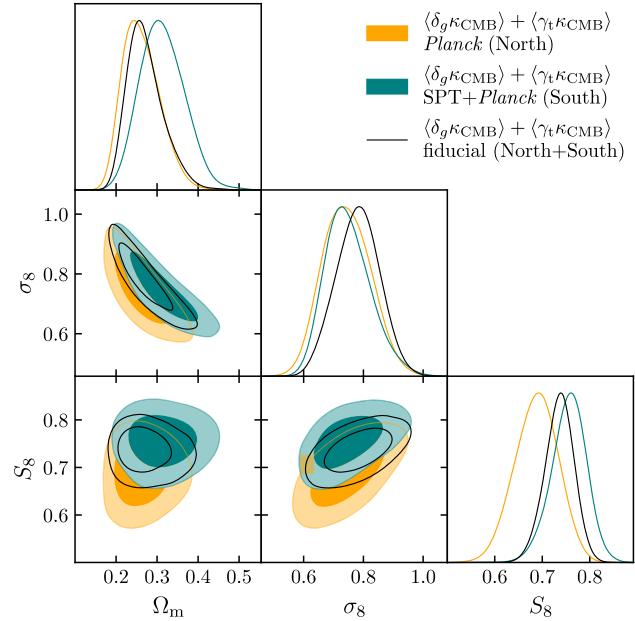
FIG. 4.   Constraints on cosmological parameters Ω_m, σ_8, and S_8 using the $\langle \delta_g \kappa_{CMB} \rangle + \langle \gamma_t \kappa_{CMB} \rangle$ probes. We also show the constraints only using the SPT + Planck area and only using the Planck area.
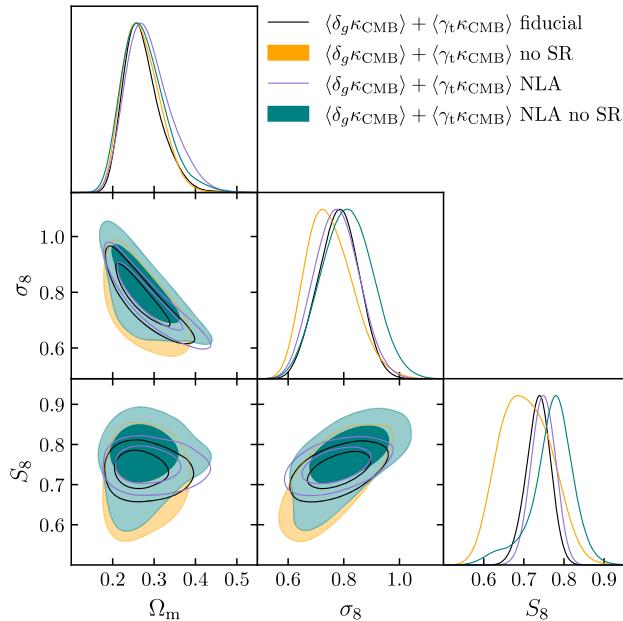
FIG. 5. Constraints on cosmological parameters Ω_m, σ_8, and S_8 using the $\langle \delta_g \kappa_{CMB} \rangle + \langle \gamma_t \kappa_{CMB} \rangle$ probes with and without including the lensing ratio (SR) likelihood, and when assuming the NLA IA model instead of our fiducial IA model TATT.

more restrictive IA model, the NLA model (see Sec. II). These results are shown in Fig. 5.

We make several observations from Fig. 5. First, the lensing ratio significantly tightens the constraints in the S_8 direction (roughly a factor of 2), as expected from Paper I. Second, without the lensing ratio, different IA models result in different S_8 constraints, with TATT resulting in ~40% larger uncertainties than NLA. This is expected given that TATT is a more general model with three more free parameters to marginalize over compared to NLA. That being said, the constraints are still fully consistent when using the different IA models. Third, when lensing ratio is included, there is very little difference in the constraints between the two different IA models. This suggests that the IA constraints coming from the lensing ratio are sufficient to make the final constraints insensitive to the particular IA model of choice.

Finally, it is interesting to look at the constraints on the IA parameters for our fiducial $\langle \delta_g \kappa_{CMB} \rangle + \langle \gamma_t \kappa_{CMB} \rangle$ analysis with and without the lensing ratio. We show this in Fig. 6, and compare them with constraints from cosmic shear [62,63] and 3 × 2 pt [16]. We find two noticeable degeneracies in these parameters:

(i) The lensing ratio restricts the $a_1 - a_2$ parameter space to a narrow band. This is seen in the cosmic shear and 3 × 2 pt results, as well as the $\langle \delta_g \kappa_{CMB} \rangle + \langle \gamma_t \kappa_{CMB} \rangle$ results, although $\langle \delta_g \kappa_{CMB} \rangle + \langle \gamma_t \kappa_{CMB} \rangle$ prefers somewhat higher a_2 values.

(ii) There is a noticeable $\eta_1 - \eta_2$ degeneracy that shows up uniquely in $\langle \delta_g \kappa_{CMB} \rangle + \langle \gamma_t \kappa_{CMB} \rangle$ and not in the

other probes in the plot. We note that this degeneracy is likely sourced by the lensing ratio likelihood, which on its own is degenerate in the $\eta_1 - \eta_2$ plane. This is consistent with what we have seen in the simulations in Paper I. The fact that it appears more prominent in $\langle \delta_g \kappa_{CMB} \rangle + \langle \gamma_t \kappa_{CMB} \rangle$ than in the other probes is partly related to the fact that a_1 and a_2 are constrained to be further away from zero in the case of $\langle \delta_g \kappa_{CMB} \rangle + \langle \gamma_t \kappa_{CMB} \rangle$, allowing η_1 and η_2 (the redshift evolution of the terms associated with a_1 and a_2) to be constrained better. Another relevant factor is that $\langle \delta_g \kappa_{CMB} \rangle + \langle \gamma_t \kappa_{CMB} \rangle$ probes slightly larger redshift ranges than cosmic shear and 3 × 2 pt due to the CMB lensing kernal, which allows for a longer redshift lever arm to constrain η_1 and η_2, resulting in qualitatively different behaviors in the $\eta_1 - \eta_2$ parameter space.

C. Nonlinear galaxy bias

As discussed in Sec. II, we test a nonlinear galaxy bias model in addition to our baseline linear galaxy bias analysis. With a nonlinear galaxy bias model we are able to use somewhat smaller scales and utilize more signal in the data (see Table II). In Fig. 7 we show the cosmological constraints of our fiducial $\langle \delta_g \kappa_{CMB} \rangle + \langle \gamma_t \kappa_{CMB} \rangle$ data vector with the nonlinear galaxy bias model. We find that the constraints between the two different galaxy bias models are consistent. There is a small improvement in the Ω_m direction, which is not surprising given that nonlinear bias impacts $\langle \delta_g \kappa_{CMB} \rangle$, and $\langle \delta_g \kappa_{CMB} \rangle$ improves the Ω_m constraints relative to $\langle \gamma_t \kappa_{CMB} \rangle$ alone. The overall improvement is nevertheless not very significant, as $\langle \gamma_t \kappa_{CMB} \rangle$ is dominating the constraints.

D. Comparison with alternative lens choices

We have defined our fiducial lens sample to be the first four bins of the MAGLIM sample. This choice is informed by the 3 × 2 pt analysis in [16], where alternative lens samples were also tested but were deemed to be potentially contaminated by systematic effects and therefore not used in the final cosmology analysis. Here, we examine the $\langle \delta_g \kappa_{CMB} \rangle + \langle \gamma_t \kappa_{CMB} \rangle$ constraints using the two alternative choices for lenses: (1) including the two high-redshift bins in MAGLIM to form a 6-bin MAGLIM sample, and (2) the REDMAGIC lens sample. As we have emphasized throughout the paper, since the galaxy-CMB lensing cross-correlation is in principle less sensitive to some of the systematic effects, these tests could potentially shed light on the issues seen in [16]. We only examine the $\langle \delta_g \kappa_{CMB} \rangle + \langle \gamma_t \kappa_{CMB} \rangle$ constraints here, but will carry out a more extensive investigation in combination with the 3 × 2 pt probes in Paper III.

In Fig. 8 we show constraints from $\langle \delta_g \kappa_{CMB} \rangle + \langle \gamma_t \kappa_{CMB} \rangle$ using the three different lens samples: 4-bin MAGLIM
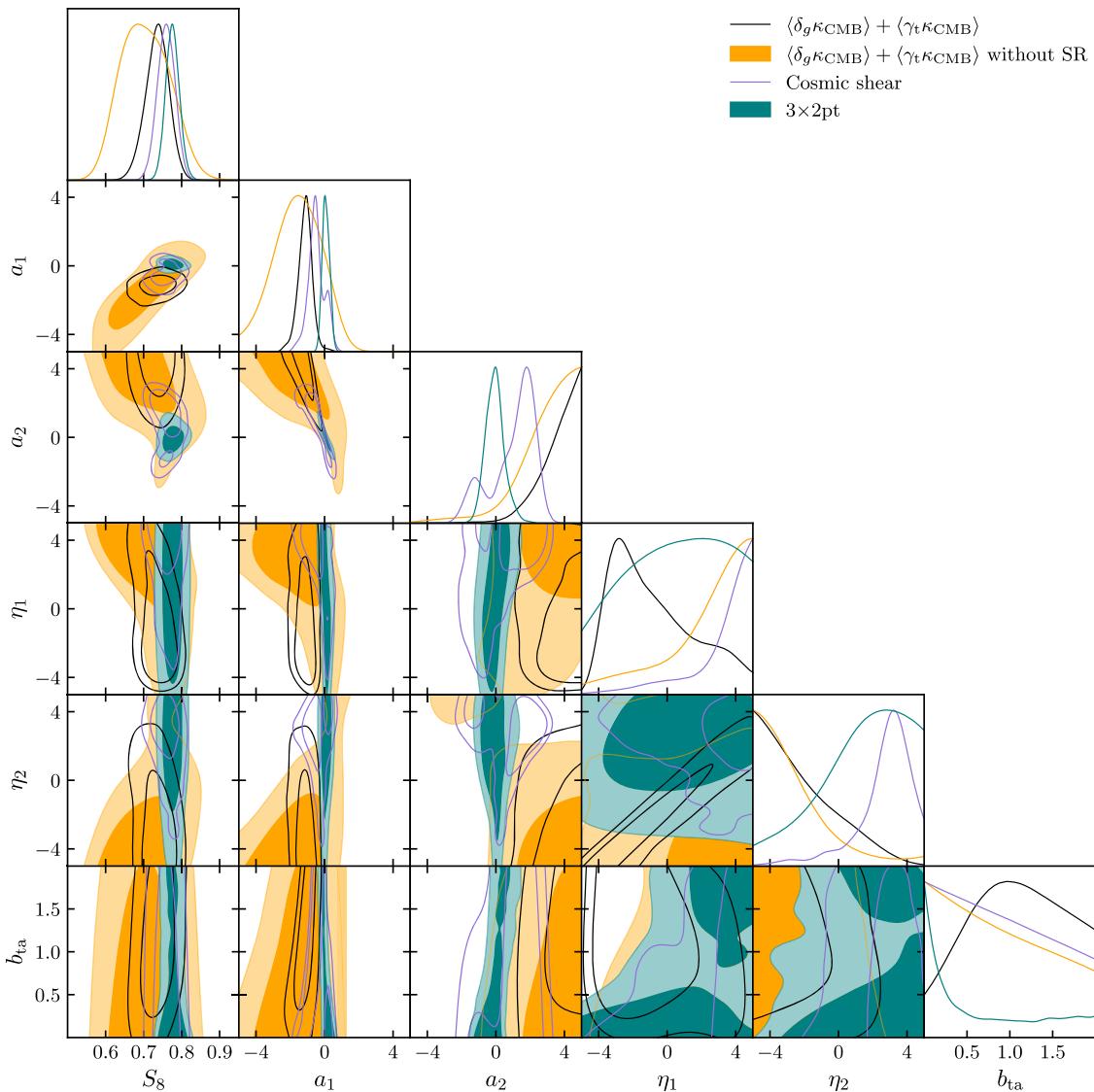
FIG. 6. Constraints on S_8 and the IA parameters from our fiducial $\langle \delta_g \kappa_{\rm CMB} \rangle + \langle \gamma_t \kappa_{\rm CMB} \rangle$ results, cosmic shear and 3 × 2 pt. We also include the $\langle \delta_g \kappa_{\rm CMB} \rangle + \langle \gamma_t \kappa_{\rm CMB} \rangle$ constraints without the lensing ratio (SR) likelihood for comparison.

(fiducial), 6-bin MAGLIM and REDMAGIC. The best-fit parameters as well as the goodness-of-fit are listed in Table III. Broadly, all three constraints appear to be very consistent with each other. This is not surprising given that the constraining power is dominated by $\langle \gamma_t \kappa_{\rm CMB} \rangle$ as we discussed earlier. In [16] it was shown that for the 3 × 2 pt analysis, both the 6-bin MAGLIM and the REDMAGIC samples give goodness-of-fits that fail our criteria, while for $\langle \delta_g \kappa_{\rm CMB} \rangle + \langle \gamma_t \kappa_{\rm CMB} \rangle$ all three samples give acceptable goodness-of-fits values as seen in Table III. This could imply that the systematic effects that contaminated the other correlation functions in 3 × 2 pt are not affecting the $\langle \delta_g \kappa_{\rm CMB} \rangle + \langle \gamma_t \kappa_{\rm CMB} \rangle$ results strongly. Compared to the fiducial constraints, the constraining power of the 6-bin MAGLIM sample is slightly higher in the Ω_m direction due to the added signal-to-noise from the high-redshift bins, while

the constraining power of the REDMAGIC sample is slightly lower in both Ω_m and S_8.

The DES Y3 3 × 2 pt analyses found that the poor fits for the alternative lens samples can be explained by inconsistent galaxy bias between galaxy-galaxy lensing $\langle \delta_g \gamma_t \rangle$ and galaxy clustering $\langle \delta_g \delta_g \rangle$. That is, when allowing the galaxy bias to be different in galaxy-galaxy lensing and galaxy clustering, the goodness-of-fit improves significantly. Operationally, this is achieved in [16] by adding a free parameter $X_{\rm lens}$, defined such that

$$X^i_{\rm lens} \times b^i_{\langle \delta_g \gamma_t \rangle} = b^i_{\langle \delta_g \delta_g \rangle}; \qquad (18)$$

where $b^i_{\langle \delta_g \gamma_t \rangle}$ ($b^i_{\langle \delta_g \delta_g \rangle}$) is the linear galaxy bias parameter for $\langle \delta_g \gamma_t \rangle$ ($\langle \delta_g \delta_g \rangle$) in lens galaxy redshift bin i. $X_{\rm lens}$ is expected
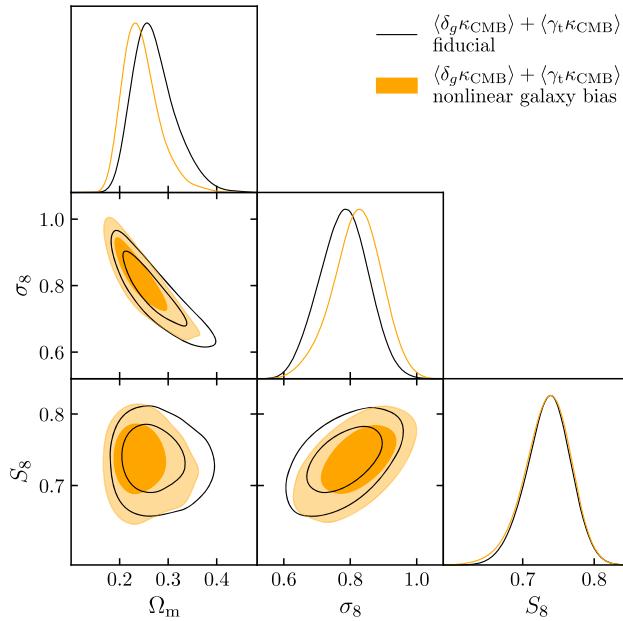
FIG. 7. Fiducial $\langle\delta_g\kappa_{CMB}\rangle + \langle\gamma_t\kappa_{CMB}\rangle$ constraints on cosmological parameters Ω_m, σ_8, and S_8 using linear and nonlinear galaxy bias models.
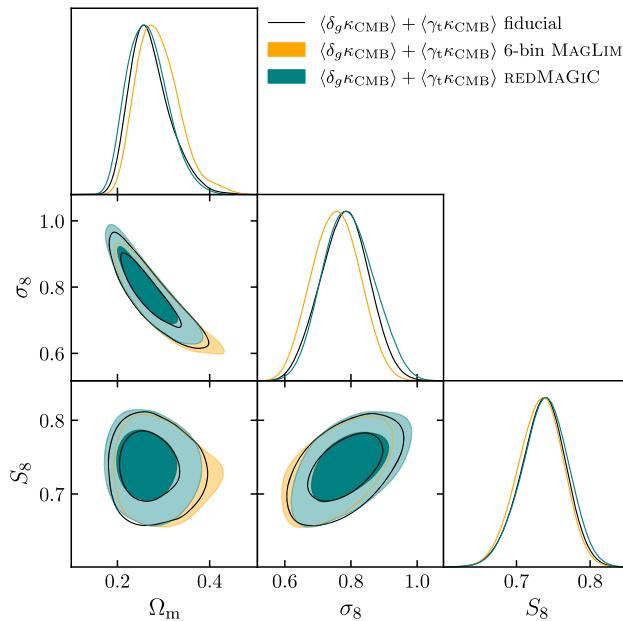
FIG. 8. Fiducial constraints on cosmological parameters Ω_m, σ_8, and S_8 using the $\langle\delta_g\kappa_{CMB}\rangle + \langle\gamma_t\kappa_{CMB}\rangle$ probes compared with using the REDMAGIC lens sample instead of the MAGLIM lens sample.

to equal 1 in the case of no significant systematic effects. In [16] it was found that $X_{lens} \neq 1$ for the two high-redshift bins in the MAGLIM sample and for all bins in the REDMAGIC sample, though there was not enough information to determine whether the systematic effect was in $\langle\delta_g\gamma_t\rangle$ or $\langle\delta_g\delta_g\rangle$.

Our CMB lensing cross-correlation analysis provides an interesting way to explore this systematic effect. In essence, with fixed cosmology, we can fit for galaxy bias using $\langle\delta_g\kappa_{CMB}\rangle$ and compare with the galaxy bias derived from $\langle\delta_g\gamma_t\rangle$ and $\langle\delta_g\delta_g\rangle$. Our results are shown in Fig. 9. We find that in general the constraints from $\langle\delta_g\kappa_{CMB}\rangle$ on galaxy bias are weaker than both galaxy-galaxy lensing and galaxy clustering, this is expected due to the lower signal-to-noise. As such, the $\langle\delta_g\kappa_{CMB}\rangle$-inferred galaxy bias values are largely consistent with both galaxy-galaxy lensing and galaxy clustering. There are a few bins, though, where $\langle\delta_g\kappa_{CMB}\rangle$ does show a preference for the galaxy bias values to agree more with one of the two probes. Noticeably, for the last two MAGLIM bins, $\langle\delta_g\kappa_{CMB}\rangle$ prefers a galaxy bias value that is closer to that inferred by galaxy clustering. On the other hand, for the highest two REDMAGIC bins, $\langle\delta_g\kappa_{CMB}\rangle$ prefers galaxy bias values that are closer to galaxy-galaxy lensing. These findings are consistent with the various investigations on X_{lens} described in [34,64] and suggest potential issues in the measurements or modeling of galaxy-galaxy lensing in the two high-redshift MAGLIM bins and galaxy clustering in the REDMAGIC sample.[7] However, we caution that these results can be cosmology-dependent, and change slightly if a different cosmology is assumed.

E. Implications for S_8 tension

In Fig. 10, we compare our constraints on S_8 from $\langle\gamma_t\kappa_{CMB}\rangle$ to those from recent measurements of cosmic shear from galaxy surveys (light blue circles) as well as other recent $\langle\gamma\kappa_{CMB}\rangle$ constraints (dark blue squares). We show only the constraint from $\langle\gamma_t\kappa_{CMB}\rangle$ (rather than $\langle\delta_g\kappa_{CMB}\rangle + \langle\gamma_t\kappa_{CMB}\rangle$) since we want to compare only measurements of gravitational lensing. These lensing measurements are not sensitive to the details of galaxy bias, unlike $\langle\delta_g\kappa_{CMB}\rangle$. We see that the constraints on S_8 obtained from $\langle\gamma_t\kappa_{CMB}\rangle$ in this work (gray band) are for the first time comparable to the state-of-the-art cosmic shear measurements.

Figure 10 also shows the inferred value of S_8 from the primary CMB (black triangles), as measured by Planck [21], ACT DR4 [65], combining ACT DR4 and the Wilkinson Microwave Anisotropy Probe [WMAP, 65], and SPT-3G [66]. As discussed in several previous works [e.g., 62,63,67] and can be seen in the figure, there is a ~2.7σ tension[8] between the S_8 value inferred from cosmic

---

[7]In particular, [34] tested an alternative REDMAGIC sample and suggested potential remedies to the systematic effect in REDMAGIC that will be explored in future work.

[8]Here we are quoting the 1D parameter difference in S_8, or $(S_8^1 - S_8^2) = \sqrt{\sigma^2(S_8^1) + \sigma^2(S_8^2)}$, where the superscript 1 and 2 refer to the two datasets we are comparing.
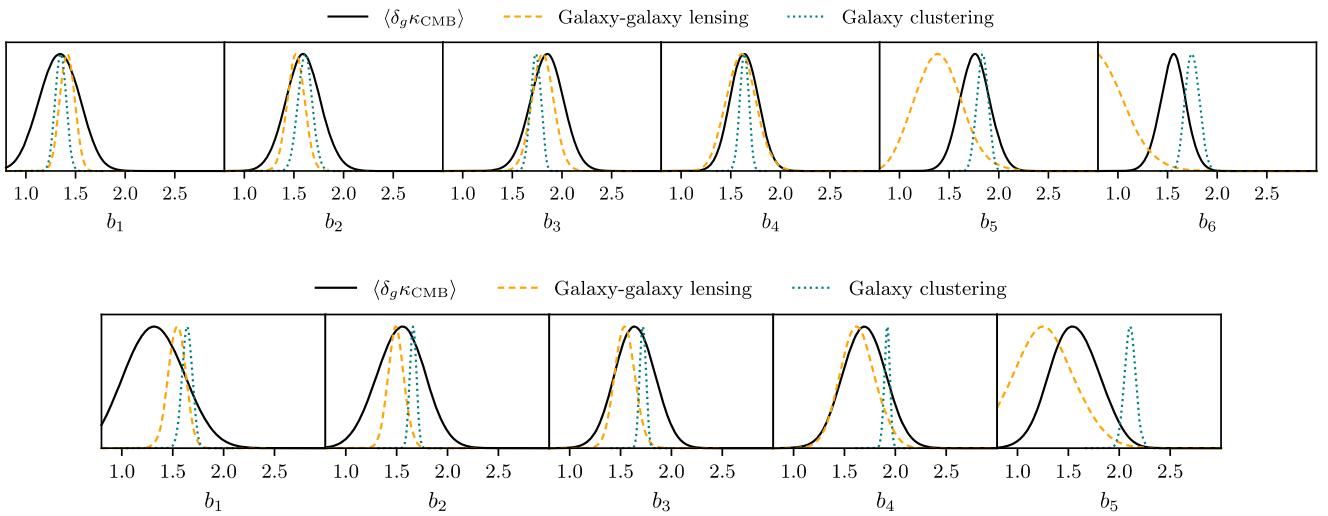
FIG. 9.   With fixed cosmological parameters, the inferred galaxy bias from $\langle\delta_g\kappa_{CMB}\rangle$, galaxy-galaxy lensing and galaxy clustering, for the MAGLIM sample (top) and the REDMAGIC sample (bottom).
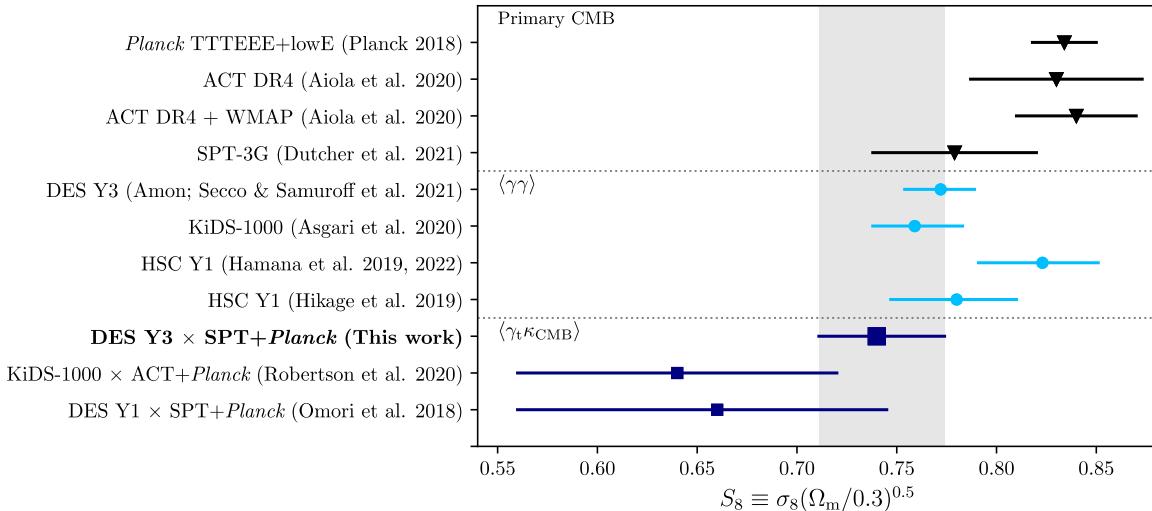
FIG. 10.   Comparison of late-time measurements of S_8 from lensing-only data (cosmic shear $\langle\gamma\gamma\rangle$ and galaxy shear-CMB lensing cross-correlation $\langle\gamma_t\kappa_{CMB}\rangle$) to the inferred value of S_8 from the primary CMB.

shear and the Planck primary CMB constraint—cosmic shear results prefer a lower S_8 value. This is intriguing given that it could indicate an inconsistency in the ΛCDM model. We also see that the other CMB datasets are currently much less constraining, but show some variation, with the lowest S_8 value from SPT-3G fairly consistent with all the cosmic shear results.

With this work, we can now meaningfully add $\langle\gamma_t\kappa_{CMB}\rangle$ into this comparison, and as we see in Fig. 10, the $\langle\gamma_t\kappa_{CMB}\rangle$ constraints on S_8 are also largely below that coming from the primary CMB. This is potentially exciting, since the $\langle\gamma_t\kappa_{CMB}\rangle$ measurements come from a cross-correlation between two very different surveys, and are therefore

expected to be highly robust to systematic errors. Our results therefore lend support to the existence of the S_8 tension. In Paper III we will perform a more rigorous and complete analysis of the consistency of our constraints here with other datasets.

VII. SUMMARY

We have presented measurements of two cross-correlations between galaxy surveys and CMB lensing: the galaxy position-CMB lensing correlation ($\langle\delta_g\kappa_{CMB}\rangle$), and the galaxy shear-CMB lensing correlation ($\langle\gamma_t\kappa_{CMB}\rangle$). These measurements are sensitive to the statistics of

large-scale structure and are additionally expected to be very robust to many observational systematics. Our measurements make use of the latest data from the first three years of observations of DES, and a new CMB lensing map constructed explicitly for cross-correlations using SPT and Planck data. In particular, our fiducial results are from four tomographic bins of the MAGLIM lens galaxy sample. The signal-to-noise of the full data vector without angular scale cuts is ~30; the part of the data vector used for cosmological inference has a signal-to-noise of ~20. The main reduction of the signal-to-noise comes from uncertainty in the modeling of nonlinear galaxy bias, which necessitates removal of the small-angle $\langle \delta_g \kappa_{CMB} \rangle$ correlation measurements. Compared to the DES Y1 analysis, the signal-to-noise increased by a factor of ~2 and we are no longer limited by contamination of tSZ in the CMB lensing map.

The joint analysis of these two cross-correlations results in the constraints $\Omega_m = 0.272^{+0.032}_{-0.052}$; $S_8 = 0.736^{+0.032}_{-0.028}$ ($\Omega_m = 0.245^{+0.026}_{-0.044}$; $S_8 = 0.734^{+0.035}_{-0.028}$) when assuming linear (nonlinear) galaxy bias in our modeling. For S_8, these constraints are more than a factor of 2 tighter than our DES Y1 results, ~30% looser than constraints from DES Y3 cosmic shear and ~70% looser than constraints from DES Y3 3 × 2 pt. We highlight here several interesting findings from this work:

  (i) We find that $\langle \gamma_t \kappa_{CMB} \rangle$ dominates the constraints in the $\langle \delta_g \kappa_{CMB} \rangle + \langle \gamma_t \kappa_{CMB} \rangle$ combination, confirming our findings from the simulated analysis in Paper I.

  (ii) We find that the lensing ratio has a large impact on the $\langle \delta_g \kappa_{CMB} \rangle + \langle \gamma_t \kappa_{CMB} \rangle$ constraints, improving the S_8 constraints by ~40%. In addition, the $\langle \delta_g \kappa_{CMB} \rangle + \langle \gamma_t \kappa_{CMB} \rangle$ data vector constrains the $\eta - \eta_2$ degeneracy direction, something not seen in the DES Y3 3 × 2 pt data vectors.

  (iii) We investigate the use of two alternative lens samples for the analysis: the 6-bin MAGLIM sample and the REDMAGIC sample. In contrast to the fiducial DES Y3 3 × 2 pt analysis, we find that the $\langle \delta_g \kappa_{CMB} \rangle + \langle \gamma_t \kappa_{CMB} \rangle$ analysis using the two alternative lens samples pass our unblinding criteria and show no signs of systematic contamination.

  (iv) With fixed cosmology, we use the $\langle \delta_g \kappa_{CMB} \rangle + \langle \gamma_t \kappa_{CMB} \rangle$ data vector to constrain the galaxy bias values using the 6-bin MAGLIM sample and the REDMAGIC sample. For the two high-redshift MAGLIM bins, we find bias values that agree more with galaxy clustering. On the other hand, for the REDMAGIC sample, we find bias values more consistent with galaxy-galaxy lensing. These provide additional information for understanding the systematic effect seen in [16] from these two alternative lens samples.

  (v) Comparing with previous cosmic shear and $\langle \gamma_t \kappa_{CMB} \rangle$ constraints, we find that in line with previous findings, our $\langle \gamma_t \kappa_{CMB} \rangle$ constraint on S_8 is lower than the primary CMB constraint from Planck. In addition, for the first time, $\langle \gamma_t \kappa_{CMB} \rangle$ has achieved comparable precision to state-of-the-art cosmic shear constraints.

The constraints derived in this paper from $\langle \delta_g \kappa_{CMB} \rangle + \langle \gamma_t \kappa_{CMB} \rangle$ can now be compared and combined with the DES Y3 3 × 2 pt probes [16], which we will do in Paper III. We will present therein our final combined results along with tests for consistency with external datasets. It is however intriguing that with the galaxy-CMB lensing cross-correlation probes alone, our datasets provide very competitive constraints on the late-time large-scale structure compared to galaxy-only probes. Due to the relative insensitivity to certain systematic effects, this additional constraint is especially important for cross-checking and significantly improving the robustness of the galaxy-only results. Another unique aspect of this work compared to other cross-correlation analyses is that we have carried out our work in an analysis framework that is fully coherent with the galaxy-only probes, making it easy to compare and combine.

Looking forward to the final datasets from DES, SPT, and ACT, as well as datasets from the Vera C. Rubin Observatory's Legacy Survey of Space and Time (LSST),[9] the ESA's Euclid mission,[10] the Roman Space Telescope,[11] the Simons Observatory (SO),[12] and CMB Stage-4[13] (CMB-S4), our results show that there are significant opportunities for combining the galaxy and CMB lensing datasets to both improve the constraints on cosmological parameters and to make the constraints themselves more robust to systematic effects.

ACKNOWLEDGMENTS

---

[9]https://www.lsst.org.
[10]https://www.euclid-ec.org.
[11]https://roman.gsfc.nasa.gov.
[12]https://simonsobservatory.org/.
[13]https://cmb-s4.org/.

APPENDIX A: JACKKNIFE COVARIANCE MATRIX

We have performed extensive validation tests on our methodology of modeling in the covariance matrix in Paper I. The ultimate check, however, is to compare the covariance matrix with a data-driven jackknife covariance matrix. The jackknife covariance incorporates naturally the noise in the data as well as any non-cosmological spatial variation in the data that might be important. This comparison was done after unblinding and the update of the covariance described in footnote 6, and is only used as a confirmation—that is, we cannot change any analysis choices based on this check.

In Fig. 11 we show the diagonal elements of the jackknife covariance matrix (calculated using the delete-one block jackknife method by dividing the footprint into 80 patches) for the fiducial lens sample, compared with our fiducial covariance matrix. We find excellent agreement between them on all scales, both in $\langle \delta_g \kappa_{CMB} \rangle$ and $\langle \gamma_t \kappa_{CMB} \rangle$, and on both the SPT þ Planck and Planck patch.
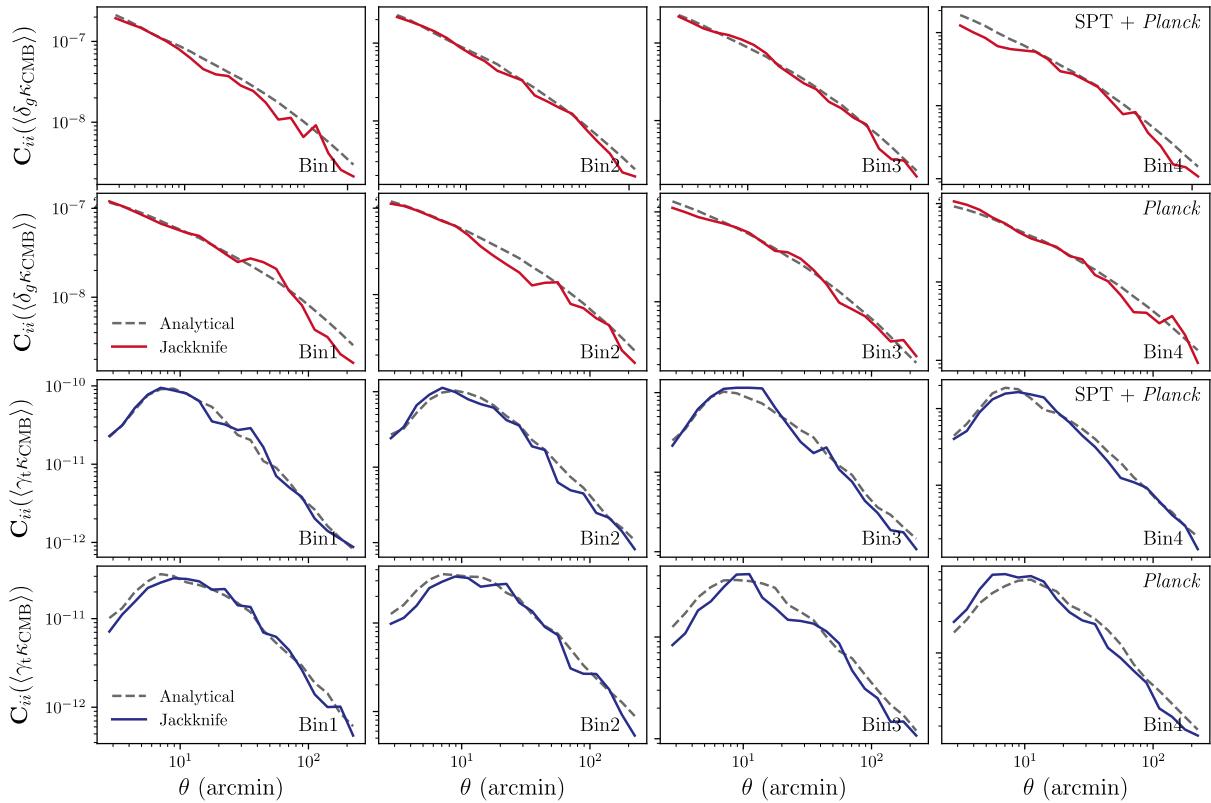
FIG. 11.   Comparison between the diagonal elements of the jackknife covariance and our fiducial covariance matrix (analytical covariance with noise-noise correction applied).

APPENDIX B: DIAGNOSTIC TESTS

We perform a number of diagnostic tests to make sure that our measurements are not significantly contaminated by potential systematic effects. As we have discussed in Sec. I, cross-survey correlations like those presented here are expected to be inherently more robust to possible systematic effects. In addition, extensive tests have been done on both the galaxy and CMB data products in [13,47,51,62,63,68]. We perform a series of diagnostic tests specific to the cross-correlation probes.

1. Cross-correlation with survey property maps

If a given contaminant associated with some survey property simultaneously affects the galaxy and the CMB fields that we are cross-correlating, the cross-correlation signal will contain a spurious component that is not cosmological. A possible example is dust, which could simultaneously contaminate the CMB lensing map (through thermal emission in CMB bands) and the galaxy density field (through extinction). In addition to dust, we consider several other possible survey properties. This test is designed to detect such effects. We calculate the correlation statistic, X_S^f, between the observables of interest and various survey property maps:

$$X_S^f(\theta) = \frac{\langle \kappa_{CMB} S(\theta) \rangle \langle f S(\theta) \rangle}{\langle S S(\theta) \rangle}; \qquad (B1)$$

where S is the survey property map of interest, and f is either δ_g or γ_t. This expression captures correlation of the systematic with both κ_{CMB} and f, and is normalized to have the same units as $\langle f \kappa_{CMB} \rangle$. Henceforth, we omit the θ-dependence in the notation for simplicity, but note that all the factors in Eq. (B1) are functions of θ. Unless the systematic map is correlated with both f and κ_{CMB}, it will not bias $\langle f \kappa_{CMB} \rangle$ and X_S^f will be consistent with zero. Note that X_S^f should also be compared with the statistical uncertainty of $\langle f \kappa_{CMB} \rangle$, as a certain systematic could be significantly detected but have little impact on the final results if it is much smaller than the statistical uncertainty.

For $\langle \delta_g \kappa_{CMB} \rangle$, we consider two S fields: stellar density and extinction. For $\langle \gamma_t \kappa_{CMB} \rangle$, we look in addition at two fields associated with PSF modeling errors. The quantities q and w measure the point-spread function (PSF) modeling residuals as introduced in [51], $q = e - e_{model}$ is the difference of the true ellipticity of the PSF as measured by stars and that inferred by the PSF model, and $w = e(T - T_{model})/T$, where T is a measure of size of the PSF, is the impact on the PSF model ellipticity when
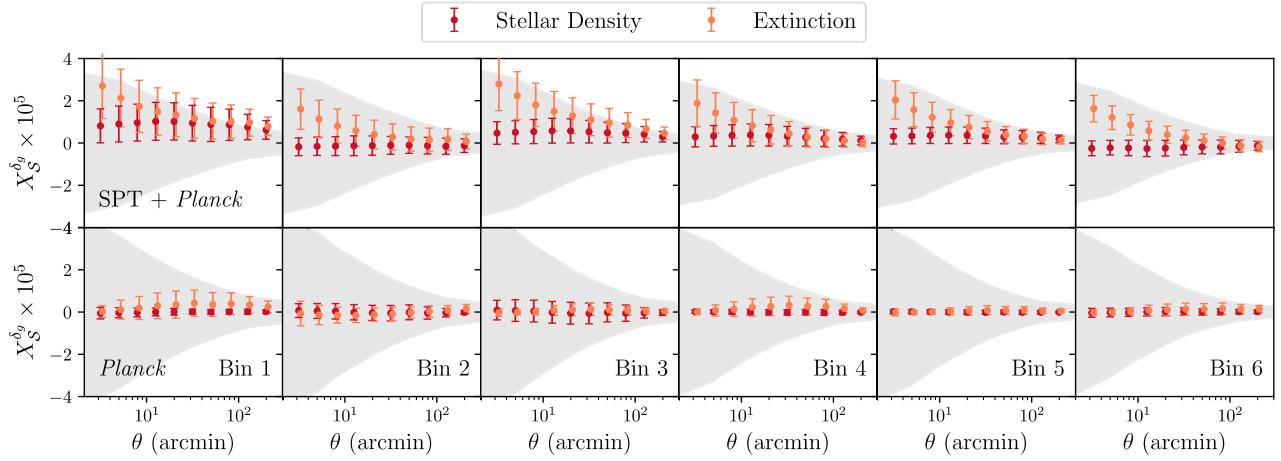
FIG. 12. The measured systematic contamination of $\langle \delta_g \kappa_{CMB} \rangle$ for the MAGLIM lens sample, as assessed by Eq. (B1), for the SPT þ Planck field (top) and the Planck field (bottom) and for different redshift bins. For reference, the gray band shows 10% of the statistical uncertainties for the corresponding data vectors. In all cases, the measured bias is significantly below the statistical uncertainties on the $\langle \delta_g \kappa_{CMB} \rangle$ measurements.
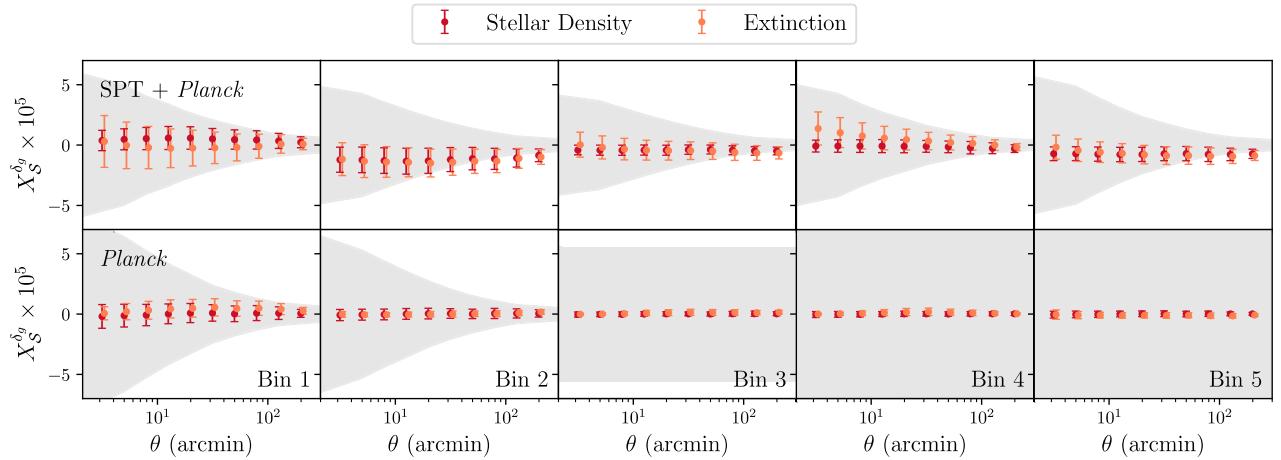

FIG. 13. Same as Fig. 12 but for the REDMAGIC lens sample.

the PSF size is wrong by $T - T_{model}$. As both q and w are spin-2 quantities like the ellipticity, we first decompose them into E and B modes using the same method used for generating weak lensing convergence maps in [69]. We then use the E-mode maps as the S maps to perform the cross-correlation test. The rationale here is that if there is a nontrivial E-mode component, it could signify contamination in the shear signal, and will correlate with the shear field.

Figures 12–14 show the result of our measured X_S^f for the different parts of the data vector. For comparison, we also plot the statistical uncertainty on the data vector; given that the statistical uncertainties are much larger than the measured biases in all cases, we scale the statistical uncertainties by 0.1 ($\langle \delta_g \kappa_{CMB} \rangle$) and 0.01 ($\langle \gamma_t \kappa_{CMB} \rangle$). The χ^2 values per degree of freedom for

the X_S^f measurements with respect to the null model are shown in Tables IV–VI together with the probability-to-exceed (PTE) values. The χ^2 as well as the error bars on the plots are derived from jackknife resampling where we use 65 equal-area jackknife patches for the SPT þ Planck footprint and 85 patches for the Planck area. To obtain a more reliable jackknife covariance, we measure X_S^f using 10 angular bins instead of the 20 bins used for the data vectors. In general, most of the systematic effects are very consistent with zero.

For $\langle \delta_g \kappa_{CMB} \rangle$, we find that the absolute level of the potential systematic effects, as quantified by X_S^f is 1-2 orders of magnitudes smaller than the statistical errors. There appears to be more cross-correlation for the SPT þ Planck area, especially with extinction. All of the PTE values of these cross-correlations are above our threshold
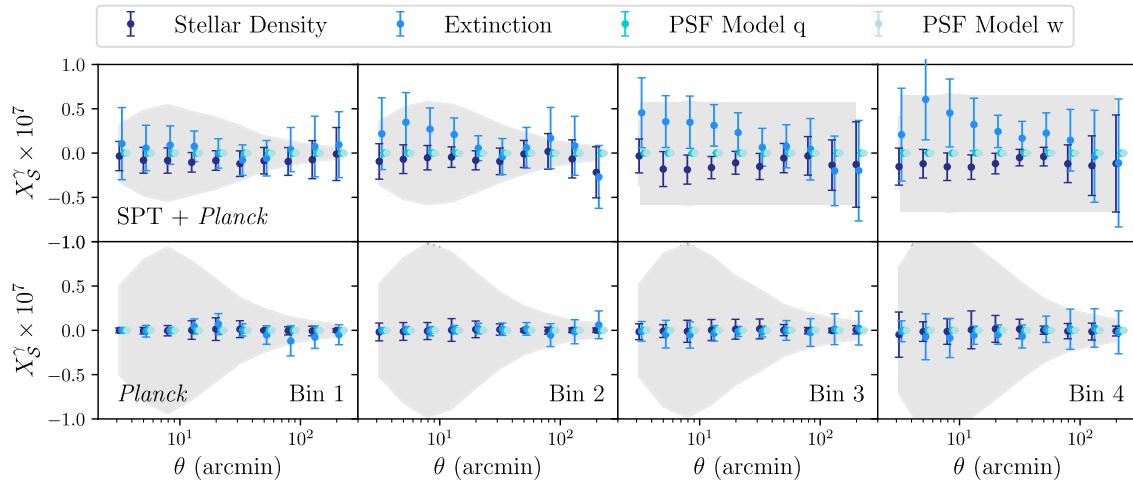
FIG. 14. The measured systematic contamination of $\langle \gamma \kappa_{CMB} \rangle$, as assessed by Eq. (B1), for the SPT þ Planck field (top) and the Planck field (bottom) and for different redshift bins. The gray band shows 1% of the statistical uncertainties for the corresponding data vectors.

for concern of 0.01, so we deem these results acceptable.

For $\langle \gamma_t \kappa_{CMB} \rangle$, we find that the absolute levels of the X_S^f measurements is much lower (> 2 orders of magnitude)— this is expected as it is much less obvious how the survey property maps will leave an imprint on the shear field. Interestingly, we also find that overall the error bars are larger in the SPT þ Planck patch compared to the Planck patch. This can be due to the survey property maps containing higher spatial fluctuation in the SPT þ Planck area as part of the footprint is close to the galactic plane or the Large Magellanic Cloud (LMC).

2. Cross-shear component

During the measurement of $\langle \gamma_t \kappa_{CMB} \rangle$, we additionally measure its cross-shear counterpart $\langle \gamma_\times \kappa_{CMB} \rangle$. We replace e_t in Eq. (16) with $e_\times$, the corrected ellipticity oriented 45° to the line connecting map pixel and the source galaxy. The correlation $\langle \gamma_\times \kappa_{CMB} \rangle$ should be consistent with zero. Any significant detection of $\langle \gamma_\times \kappa_{CMB} \rangle$ could signal systematic effects in the $\langle \gamma_t \kappa_{CMB} \rangle$ measurements.

Our results are shown in Fig. 15 with the χ^2 per degree of freedom and PTE values listed in Table VI. We find no significant detection of $\langle \gamma_\times \kappa_{CMB} \rangle$ in all parts of the data vector.

3. $\langle \delta_g \kappa_{CMB} \rangle$ measurements with and without weights

As discussed in [47], weights are applied to the lens galaxies in order to remove correlations with various survey properties. When performing the $\langle \delta_g \kappa_{CMB} \rangle$ measurement in

TABLE IV. The χ^2 per degree of freedom for the systematics diagnostics quantity [Eq (B1)] for the MAGLIM $\langle \delta_g \kappa_{CMB} \rangle$ measurements. The different columns represent the different survey properties S, whereas the different rows are for the tomographic bins in both the SPT þ Planck patch and the Planck patch. The corresponding PTE values are listed in the parentheses.

S	Stellar density	Extinction
Bin	χ^2=d:o:f: (PTE)	
SPT þ Planck		
1	0.42 (0.85)	0.90 (0.49)
2	0.10 (0.99)	0.65 (0.71)
3	0.21 (0.98)	0.64 (0.72)
4	0.13 (0.99)	1.12 (0.34)
5	0.22 (0.98)	1.34 (0.21)
6	0.36 (0.93)	1.66 (0.10)
Planck		
1	0.02 (0.99)	0.40 (0.87)
2	0.12 (0.99)	0.26 (0.96)
3	0.15 (0.99)	0.28 (0.96)
4	0.08 (0.99)	0.33 (0.93)
5	0.06 (0.99)	0.21 (0.98)
6	0.05 (0.99)	0.18 (0.98)

TABLE V. Same as Table IV but for the REDMAGIC lens sample.

S	Stellar density	Extinction
Bin	χ^2=d:o:f: (PTE)	
SPT þ Planck		
1	0.09 (0.99)	0.20 (0.97)
2	0.50 (0.83)	0.56 (0.78)
3	0.42 (0.88)	0.38 (0.91)
4	0.28 (0.96)	0.76 (0.62)
5	0.73 (0.64)	1.13 (0.33)
Planck		
1	0.09 (0.99)	0.38 (0.89)
2	0.09 (0.99)	0.16 (0.99)
3	0.05 (0.99)	0.19 (0.98)
4	0.04 (0.99)	0.16 (0.99)
5	0.04 (0.99)	0.16 (0.99)

TABLE VI. The χ^2 per degree of freedom for the systematics diagnostics quantity [Eq. (14)] for the $\langle \gamma_t \kappa_{CMB} \rangle$ measurements. The different columns represent the different survey properties S, whereas the different rows are for the tomographic bins in both the SPT þ Planck patch and the Planck patch. The corresponding PTE values are listed in the parentheses. The last column lists the corresponding numbers for the cross-shear measurement described in Sec. B 2.

	S	Stellar density	Extinction	PSF model error q	PSF model error w	$\gamma_\times$
	Bin			χ^2 =d:o:f: (PTE)		
SPT þ Planck	1	0.12 (0.99)	0.12 (0.99)	0.34 (0.96)	0.15 (0.99)	1.11 (0.34)
	2	0.17 (0.99)	0.38 (0.95)	0.20 (0.99)	0.18 (0.99)	1.18 (0.29)
	3	0.32 (0.94)	0.39 (0.90)	0.40 (0.89)	0.30 (0.95)	0.60 (0.75)
	4	0.20 (0.97)	0.41 (0.86)	0.19 (0.97)	0.15 (0.98)	1.91 (0.07)
Planck	1	0.09 (0.99)	0.06 (0.99)	0.11 (0.99)	0.08 (0.99)	1.15 (0.31)
	2	0.09 (0.99)	0.04 (0.99)	0.25 (0.98)	0.17 (0.99)	1.28 (0.23)
	3	0.12 (0.99)	0.07 (0.99)	0.19 (0.99)	0.14 (0.99)	1.16 (0.31)
	4	0.16 (0.99)	0.18 (0.99)	0.27 (0.98)	0.18 (0.99)	1.12 (0.33)

Eq. (14), these weights are applied (i.e. the w in Eq. 5). In a cross-correlation, the effect of these weights will be non-negligible if the systematic effect that is being corrected by the weights also correlates with the CMB lensing map. We note that this test is not always a null-test, as we consider it more correct to use the weights. Rather, it shows qualitatively the level of the correction from these weights—naively, the smaller the correction to start with, the less likely the residual contamination will be.

In Fig. 16 we show the difference between the $\langle \gamma_t \kappa_{CMB} \rangle$ measurements with and without using the lens weights, for the two lens samples. To understand the significance of these results, we calculate the $\Delta\chi^2$ between the data vectors with and without weights for the fiducial MAGLIM sample, using the analytic covariance for the data vector and find a $\Delta\chi^2$ of 1.23 after scale cuts. Propagating this into cosmological constraints by running two chains using $\langle \gamma_t \kappa_{CMB} \rangle$ with and without weights (fixing galaxy bias) gives a negligible 0.02σ shift in the $\Omega_m - S_8$ plane. It is also worth pointing out that we see that the weights most significantly affect the two high-redshift bins in the MAGLIM sample, this is likely due to the fact that the high-redshift bins are fainter and more affected by the spatially varying observing conditions.

4. Biases from source masking

In constructing the CMB lensing maps for this analysis, we apply a special procedure at the locations of bright point sources to reduce their impact on the output lensing maps. As described in more detail in Paper I, the CMB lensing estimator that we use involves two CMB maps, or "legs." One of these is high-resolution map (i.e. the SPT þ Planck temperature map), and the other is a low-resolution tSZ-cleaned map (i.e. the Planck SMICAnosz temperature map). To reduce the impact of point sources, we inpaint the point sources with fluxes 6.4 < F < 200 mJy using the method described in [70]. The total inpainted area is roughly 3.6% of the map. The corresponding location in the tSZ-cleaned map are left untouched. We expect this procedure to result in a reasonable estimate of κ_{CMB} at the
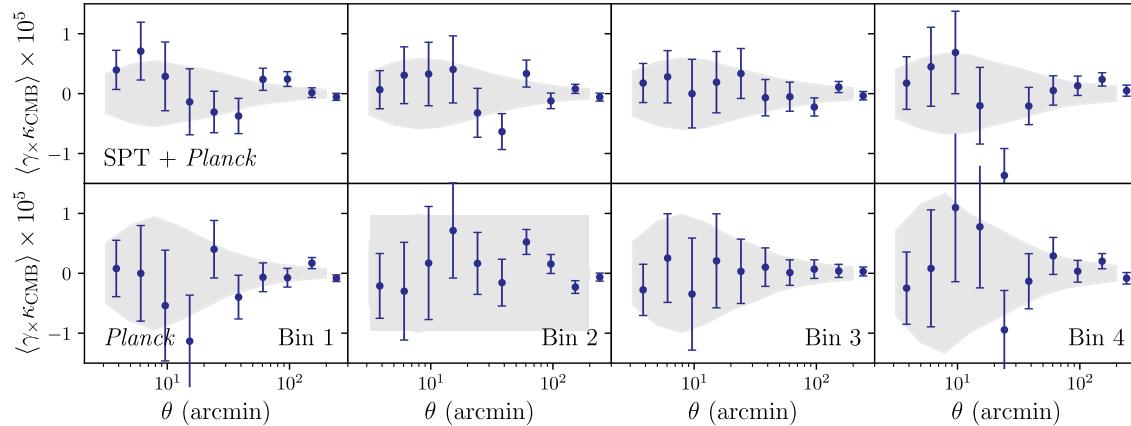

FIG. 15. Cross-correlation between than cross-component of shear with CMB lensing for the SPT þ Planck field (top) and the Planck field (bottom) and for different redshift bins. The gray band shows the statistical uncertainties for $\langle \gamma_t \kappa_{CMB} \rangle$.
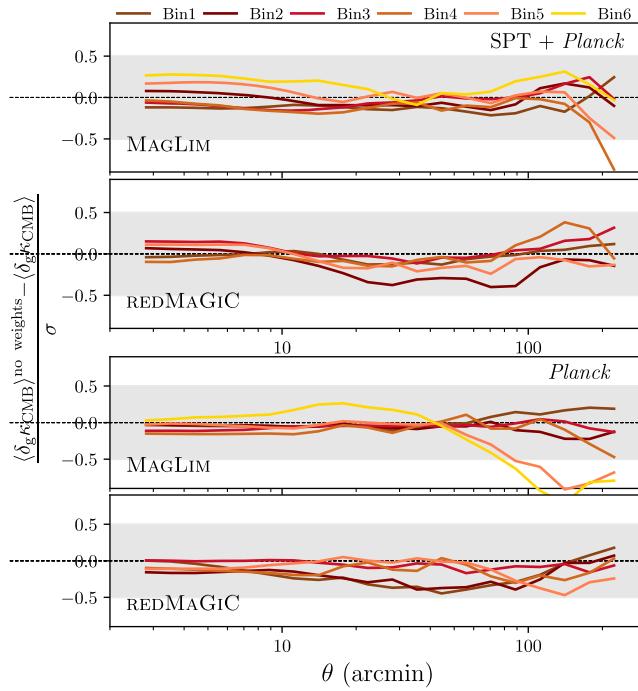
FIG. 16. The difference in the $\langle \delta_g \kappa_{CMB} \rangle$ cross-correlation between the two lens galaxy samples MAGLIM and REDMAGIC with CMB lensing when using weights and without weights, over the statistical uncertainty of the measurement σ.

locations of the point sources given that only one leg is inpainted, and the area being inpainted is small (such that Gaussian constrained inpainting predicts the pixels values of the inpainted region well) although it is possible that the noise properties of these regions differ somewhat from the map as a whole.
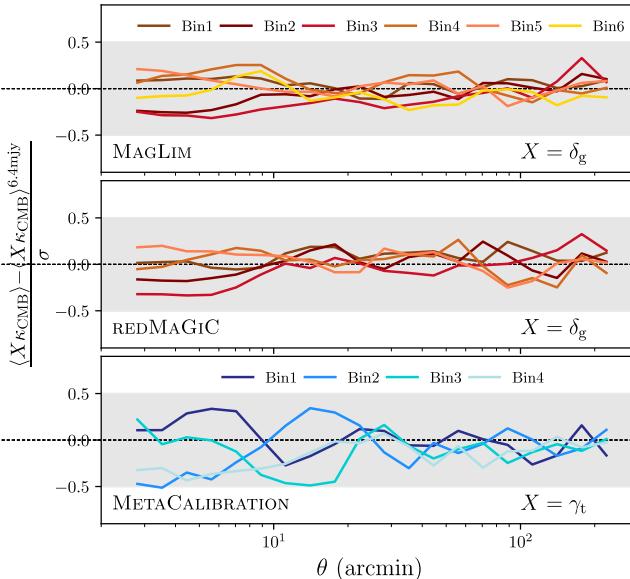

FIG. 17. Difference in the data vectors using the alternative mask and the fiducial one. This test is only done for the SPT þ Planck patch, as it is specific to the SPT lensing reconstruction.
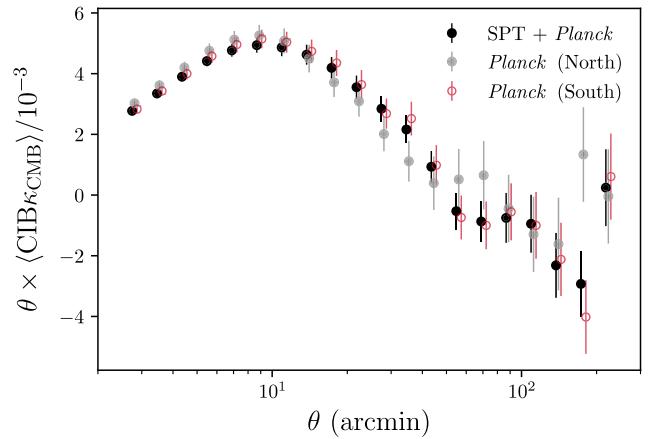

FIG. 18. Cross-correlation between CIB and the Planck lensing map in the North patch (solid gray), the Planck lensing map in the South patch (open red), and the SPT þ Planck lensing map (black).

To test whether the inpainting procedure results in any bias, we also measure the cross-correlation with the lensing map after masking (i.e. completely removing) all the point sources down to 6.4 mJy. We show in Fig. 17 the difference in the data vectors using the alternative mask and the fiducial one. We find that there is no coherent difference in the correlation measurements across the range of angular scales considered. There is, however, some scatter about our nominal measurements. The level of this scatter is small, roughly 0.25 and 0.50σ across the full range of angular scales for $\langle \delta_g \kappa_{CMB} \rangle$ and $\langle \gamma_t \kappa_{CMB} \rangle$ respectively.[14] Given that such scatter is expected to have negligible impact on our results, and since some scatter between the data points is expected simply due to the different selection of pixels in the masked and unmasked CMB lensing maps, we do not find this to be a cause for worry. Our baseline results will use the unmasked version of the CMB lensing map.

5. Variations in the CMB lensing map

Our fiducial analysis uses the SPT þ Planck map in the Dec < −40° region and the Planck lensing map in the region Dec > −39.5°. We left a 0.5° gap between the two maps to avoid correlation between the large-scale structure on the boundary. Here we like to verify that the cross-correlation of our CMB lensing maps with another large-scale structure tracer is consistent between the two patches and the two CMB lensing data sets. We choose to use the cosmic infrared background (CIB) map from [71] as this large-scale structure tracer. We carry out the following two

---

[14]This scatter results from the slightly higher-noise region caused by the half-leg lensing reconstruction, with the point sources left in the non-inpainted map effectively behaving as noise.

[15]Here we use the n_H ¼ 2.5e20 cm^{-1} maps as defined in [71].
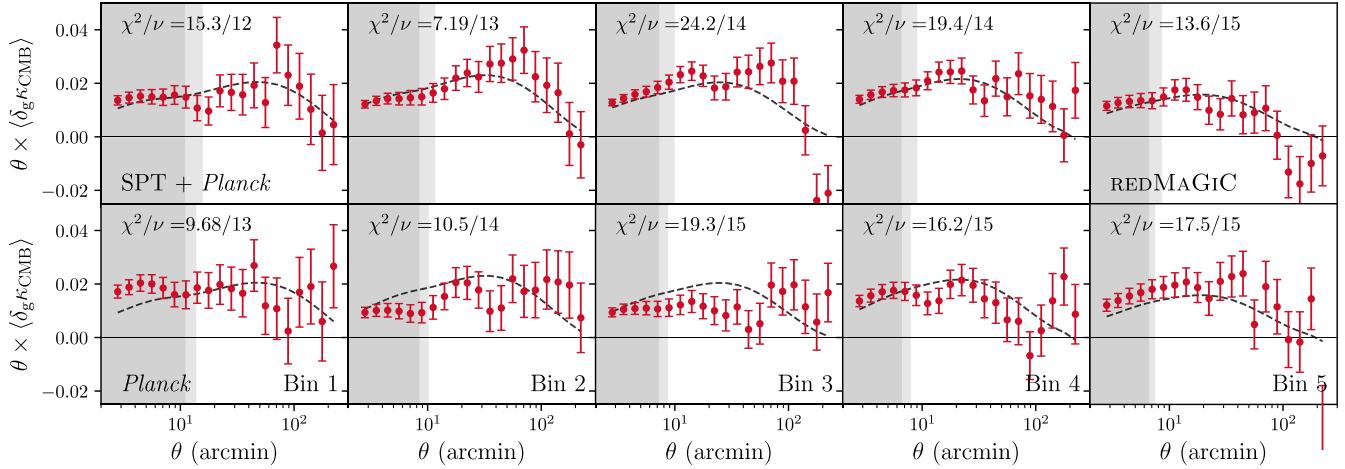
FIG. 19. Same as Fig 2 but for the REDMAGIC sample.

tests: (1) we compare the cross-correlations between the CIB map and the Planck lensing map split into two sub-regions (the "North" region with DEC > −39.5° and the "South" region with DEC < −40°), and verify that they are consistent; (2) we compare in the South patch the cross-correlations between the CIB map with either the Planck CMB lensing map or our SPT þ Planck lensing map, and verify that they are consistent.

The resulting correlation measurements are shown in Fig. 18—the high signal-to-noise is expected due to the significant overlap in the kernels of the two tracers. We make two comparisons:

(1) CIB × Planck North vs. CIB × Planck South: We find a two-sample χ^2=v of 24.28=20 with a PTE of 0.23. This demonstrates that the two patches are consistent with each other.

(2) SPT þ Planck vs. Planck South: We compute the two-sample χ^2, and find χ^2=v ¼ 23.9=20., with a PTE of 0.25. This demonstrates that the two measurements are consistent with each other.

We note that there are two caveats associated with these cross-correlation measurements. The first is that, at 545 GHz, galactic emission is non-negligible, and while the CIB maps from [71] are intended to be free of galactic dust, there may be residuals. Second, the CIB-κ_{CMB} correlation is most sensitive to redshifts higher than those probed by DES galaxies, thus we are extrapolating the results above to lower redshift.

APPENDIX C: REDMAGIC RESULTS

In this appendix we show the results for the second lens sample—the REDMAGIC sample. The data vector is shown in Fig. 19 with signal-to-noise values listed in Table II. We find that (1) no significant systematic effects were found as described in Appendix B, (2) we get a p-value greater than 0.01 when comparing the h$\delta_g\kappa_{CMB}$i þ h$\gamma_t\kappa_{CMB}$i constraints from Planck to constraints from SPT þ Planck, and (3) the goodness-of-fit of the fiducial h$\delta_g\kappa_{CMB}$i þ h$\gamma_t\kappa_{CMB}$i unblinded chain corresponds to a p-value greater than 0.01. These results allowed us to unblind our results, and the final constraints are listed in Table III and the fiducial constraints are shown in Fig 8.

[1] B. Flaugher, H. T. Diehl, K. Honscheid et al. (DES Collaboration), Astron. J. 150, 150 (2015).

[2] J. E. Carlstrom, P. A. R. Ade, K. A. Aird et al., Publ. Astron. Soc. Pac. 123, 568 (2011).

[3] B. Soergel, S. Flender, K. T. Story et al., Mon. Not. R. Astron. Soc. 461, 3172 (2016).

[4] D. Kirk, Y. Omori, A. Benoit-Lévy et al., Mon. Not. R. Astron. Soc. 459, 21 (2016).

[5] T. Giannantonio, P. Fosalba, R. Cawthon et al., Mon. Not. R. Astron. Soc. 456, 3213 (2016).

[6] E. Baxter, J. Clampitt, T. Giannantonio et al., Mon. Not. R. Astron. Soc. 461, 4099 (2016).

[7] E. J. Baxter, S. Raghunathan, T. M. Crawford et al., Mon. Not. R. Astron. Soc. 476, 2674 (2018).

[8] J. Prat, E. Baxter, T. Shin et al., Mon. Not. R. Astron. Soc. 487, 1363 (2019).

[9] Y. Omori, T. Giannantonio, A. Porredon et al., Phys. Rev. D 100, 043501 (2019).

[10] Y. Omori, E. J. Baxter, C. Chang et al., Phys Rev. D 100, 043517 (2019).

[11] T. M. C. Abbott et al. (DES and SPT Collaborations), Phys. Rev. D 100, 023541 (2019).

[12] M. Costanzi, A. Saro, S. Bocquet et al., Phys. Rev. D 103, 043522 (2021).

[13] Y. Omori, R. Chown, G. Simard et al., Astrophys. J. 849, 124 (2017).

[14] N. Aghanim, Y. Akrami et al. (Planck Collaboration), Astron. Astrophys. 641, A8 (2020).

[15] Y. Omori et al., preceding paper, Phys. Rev. D 107, 023529 (2023).

[16] T. M. C. Abbott et al. (DES Collaboration) Phys. Rev. D 105, 023520 (2022).

[17] C. Sánchez, J. Prat, G. Zacharegkas et al., Phys. Rev. D 105, 083529 (2022).

[18] T. M. C. Abbott et al. (DES and SPT Collaborations), following paper, Phys. Rev. D 107, 023531 (2022).

[19] G. A. Marques, J. Liu, K. M. Huffenberger, and J. C. Hill, Astrophys. J. 904, 182 (2020).

[20] H. Aihara, N. Arimoto, R. Armstrong et al., Publ. Astron. Soc. Jpn. 70, S4 (2018).

[21] P. A. R. Ade, N. Aghanim et al. (Planck Collaboration), Astron. Astrophys. 594, A15 (2016).

[22] T. Namikawa, Y. Chinone, H. Miyatake et al., Astrophys. J. 882, 62 (2019).

[23] Z. D. Kermish, P. Ade, A. Anthony et al., Proc. SPIE Int. Soc. Opt. Eng. 8452, 1C (2012).

[24] N. C. Robertson, D. Alonso, J. Harnois-Déraps et al., Astron. Astrophys. 649, A146 (2021).

[25] J. T. A. de Jong, G. A. Verdoes Kleijn, K. H. Kuijken et al., Exp. Astron. 35, 25 (2013).

[26] D. S. Swetz, P. A. R. Ade, M. Amiri et al., Astrophys. J. Suppl. Ser. 194, 41 (2011).

[27] A. Krolewski, S. Ferraro, and M. White, J. Cosmol. Astropart. Phys. 12 (2021) 028.

[28] E. F. Schlafly, A. M. Meisner, and G. M. Green, Astrophys. J. Suppl. Ser. 240, 30 (2019).

[29] E. Krause, X. Fang, S. Pandey et al., arXiv:2105.13548.

[30] X. Fang, E. Krause, T. Eifler, and N. MacCrann, J. Cosmol. Astropart. Phys. 05 (2020) 010.

[31] D. N. Limber, Astrophys. J. 117, 134 (1953).

[32] A. Lewis, A. Challinor, and A. Lasenby, Astrophys. J. 538, 473 (2000).

[33] R. Takahashi, M. Sato, T. Nishimichi, A. Taruya, and M. Oguri, Astrophys. J. 761, 152 (2012).

[34] S. Pandey, E. Krause, J. DeRose et al., Phys. Rev. D 106, 043520 (2022).

[35] J. A. Blazek, N. MacCrann, M. A. Troxel, and X. Fang, Phys. Rev. D 100, 103506 (2019).

[36] S. Bridle and L. King, New J. Phys. 9, 444 (2007).

[37] J. Elvin-Poole, N. MacCrann et al., arXiv:2209.09782.

[38] R. Cawthon et al. (DES Collaboration), Mon. Not. R. Astron. Soc. 513, 5517 (2022), arXiv:2012.12826.

[39] C.-H. Lin, J. Harnois-Déraps, T. Eifler, T. Pospisil, R. Mandelbaum, A. B. Lee, and S. Singh, Mon. Not. R. Astron. Soc. 499, 2977 (2020).

[40] J. Zuntz, M. Paterno, E. Jennings et al., Astron. Comput. 12, 45 (2015).

[41] W. J. Handley, M. P. Hobson, and A. N. Lasenby, Mon. Not. R. Astron. Soc. 453, 4384 (2015).

[42] M. S. Madhavacheril and J. C. Hill, Phys. Rev. D 98, 023534 (2018).

[43] B. Flaugher, Int. J. Mod. Phys. A 20, 3121 (2005).

[44] I. Sevilla-Noarbe, K. Bechtol, M. Carrasco Kind et al., Astrophys. J. Suppl. Ser. 254, 24 (2021).

[45] J. De Vicente, E. Sánchez, and I. Sevilla-Noarbe, Mon. Not. R. Astron. Soc. 459, 3078 (2016).

[46] A. Porredon et al. (DES Collaboration), Phys. Rev. D 103, 043503 (2021).

[47] M. Rodríguez-Monroy, N. Weaverdyck, J. Elvin-Poole et al., Mon. Not. R. Astron. Soc. 511, 2665 (2022).

[48] E. Rozo, E. S. Rykoff, A. Abate et al., Mon. Not. R. Astron. Soc. 461, 1431 (2016).

[49] E. S. Rykoff, E. Rozo, M. T. Busha et al., Astrophys. J. 785, 104 (2014).

[50] E. S. Rykoff, E. Rozo, D. Hollowood et al., Astrophys. J. Suppl. Ser. 224, 1 (2016).

[51] M. Gatti, E. Sheldon, A. Amon et al., Mon. Not. R. Astron. Soc. 504, 4312 (2021).

[52] E. Huff and R. Mandelbaum, arXiv:1702.02600.

[53] E. S. Sheldon and E. M. Huff, Astrophys. J. 841, 24 (2017).

[54] N. MacCrann, M. R. Becker, J. McCullough et al., Mon. Not. R. Astron. Soc. 509, 3371 (2022).

[55] J. Myles, A. Alarcon, A. Amon et al., Mon. Not. R. Astron. Soc. 505, 4249 (2021).

[56] W. G. Hartley, A. Choi, A. Amon et al., Mon. Not. R. Astron. Soc. 509, 3547 (2022).

[57] S. Everett, B. Yanny, N. Kuropatkin et al., Astrophys. J. Suppl. Ser. 258, 15 (2022).

[58] M. Gatti, G. Giannini, G. M. Bernstein et al., Mon. Not. R. Astron. Soc. 510, 1223 (2022).

[59] M. Jarvis, G. Bernstein, and B. Jain, Mon. Not. R. Astron. Soc. 352, 338 (2004).

[60] J. Muir, G. M. Bernstein, D. Huterer et al., Mon. Not. R. Astron. Soc. 494, 4454 (2020).

[61] C. Doux, E. Baxter, P. Lemos et al., Mon. Not. R. Astron. Soc. 503, 2688 (2021).

[62] A. Amon, D. Gruen, M. A. Troxel et al., Phys. Rev. D 105, 023514 (2022).

[63] L. F. Secco, S. Samuroff, E. Krause et al., Phys. Rev. D 105, 023515 (2022).

[64] A. Porredon, M. Crocce, J. Elvin-Poole et al., arXiv:2105.13546.

[65] S. Aiola, E. Calabrese, L. Maurin et al., J. Cosmol. Astropart. Phys. 12 (2020) 047.

[66] D. Dutcher, L. Balkenhol, P. A. R. Ade et al., Phys. Rev. D 104, 022003 (2021).

[67] M. Asgari, C. Heymans, H. Hildebrandt et al., Astron. Astrophys. 624, A134 (2019).

[68] J. Prat, J. Blazek, C. Sánchez et al., Phys. Rev. D 105, 083528 (2022).

[69] N. Jeffrey, M. Gatti, C. Chang et al., Mon. Not. R. Astron. Soc. 505, 4626 (2021).

[70] A. Benoit-Lévy, T. Déchelette, K. Benabed, J.-F. Cardoso, D. Hanson, and S. Prunet, Astron. Astrophys. 555, A37 (2013).

[71] D. Lenz, O. Doré, and G. Lagache, Astrophys. J. 883, 75 (2019).